

Estimation of Synaptic Conductance in the Spiking Regime for the McKean Neuron Model*

A. Guillamon[†], R. Prohens[‡], A. E. Teruel[‡], and C. Vich[‡]

Abstract. In this work, we aim at giving a first proof of concept to address the estimation of synaptic conductances when a neuron is spiking, a complex inverse nonlinear problem which is an open challenge in neuroscience. Our approach is based on a simplified model of neuronal activity, namely, a piecewise linear version of the FitzHugh–Nagumo model. This simplified model allows precise knowledge of the nonlinear f-I curve by using standard techniques of nonsmooth dynamical systems. In the regular firing regime of the neuron model, we obtain an approximation of the period which, in addition, improves previous approximations given in the literature to date. By knowing both this expression of the period and the current applied to the neuron, and then solving an inverse problem with a unique solution, we are able to estimate the steady synaptic conductance of the cell's oscillatory activity. Moreover, the method gives also good estimations when the synaptic conductance varies slowly in time.

Key words. McKean model, synaptic conductance, neuron model, piecewise linear system, parameter estimation, spiking neuron

AMS subject classifications. Primary, 37N25, 70K70; Secondary, 34D15, 34C25, 34C26

DOI. 10.1137/16M1088326

1. Introduction. Estimating the synaptic conductances impinging on a single neuron directly from its membrane potential is one of the open problems that needs to be solved in order to understand the flow of information in the brain. The ultimate goal is providing useful methods to deal with experimental data and give trustable estimations of excitatory and inhibitory currents arriving to a neuron. These input estimations constitute an important piece of information to understand the organization of activity in the populations of efferent neurons. In particular, they can shed light on the excitation versus inhibition balance through time in the subjacent network (see the introduction of [4] and [26] for specific applications).

Broadly speaking, there are three main obstacles to overcome in order to provide effective solutions to this inverse problem. On one hand, one needs a mathematical model of the target neuron in which the synaptic conductances are well identified (generally, as parameters of the

*Received by the editors August 5, 2016; accepted for publication (in revised form) by C. Chow March 13, 2017; published electronically August 1, 2017.

<http://www.siam.org/journals/siads/16-3/M108832.html>

Funding: The work of the second, third, and fourth authors was partially supported by the Spanish Ministry of Economy and Competitiveness through the MINECO/FEDER project MTM2014-54275-P. The work of the first and fourth authors was supported by the MINECO/FEDER project MTM2015-71509-C2-2-R. The work of the first author was supported by the Government of Catalonia under grant 2014-SGR-504.

[†]Departament de Matemàtiques, EPSEB, Universitat Politècnica de Catalunya, Spain (antoni.guillamon@upc.edu).

[‡]Departament de Matemàtiques i Informàtica, Universitat de les Illes Balears, Spain (rafel.prohens@uib.cat, antonioe.teruel@uib.es, catalina.vich@uib.es).

system). Aiming at giving methods as general as possible, the variety of neuron types does not advise the use of very specific models, but rather minimal models that capture essential features of neuronal dynamics. This idea has been extensively used in the existing literature (see [5], [2], [27], [22], [20], [3], [4], among others) assuming that data is following some underlying linear process. Normally, this assumption involves a complementary treatment of the noise present in the data, which is the second main obstacle. Some strategies consists of filtering the data before fitting them to the “minimal model” (see [2], [5], among others), and some use stochastic linear processes in order to obtain the estimations (see [22], [20], [19], [4], among others). Other approaches use more sophisticated filtering techniques (see [15], [9], [6], among others). In all these stochastic approaches, linear regression methods and maximum likelihood estimators are in order at some point of the procedure. Despite some excellent estimations obtained in particular circumstances, especially in purely leaky subthreshold regimes, misestimations derived from the use of linear models have also been reported (see [5], [13], [26]). Therefore, a third challenge, related to the type of minimal models to use, comes into play. The problem is how to deal with the inverse estimation problem when the underlying (deterministic) model is no longer linear. A partial solution for subthreshold regimes with active (nonlinearly behaving) ionic currents has been given in [26], but no solution for spiking neurons have yet been proposed.

In this work, we provide a first proof of concept to perform estimations of synaptic conductances during spiking activity. We approach this problem by considering the neuronal firing rate, f , as a function of the input current, I , i.e., the spike frequency f versus the input strength current I function (known as the f - I curve). We have chosen the McKean model, a simplified piecewise linear model of neuronal activity with regular firing, that can be derived from the FitzHugh–Nagumo model (see [17] and [7]). The piecewise linearity of the vector field allows very precise knowledge of the nonlinear f - I curve by means of standard techniques of nonsmooth dynamical systems. In the standard McKean model, we put special emphasis on the synaptic current, $I_{syn}(v)$. We consider the piecewise linear differential system

$$(1) \quad \begin{cases} C\dot{v} = f(v) - w - w_0 + I_{total}, \\ \dot{w} = v - \gamma w - v_0, \end{cases}$$

where $I_{total} = I - I_{syn}(v)$, $I_{syn}(v) = g_{syn}(v - v_{syn})$ and $f(v)$ is the piecewise linear caricature of the cubic FitzHugh–Nagumo function given by

$$f(v) = \begin{cases} -v, & v < a/2, \\ v - a, & a/2 \leq v \leq (1+a)/2, \\ 1 - v, & v > (1+a)/2. \end{cases}$$

Physiologically, the variables of the model are considered to be v , which stands for the membrane potential, and w , which represents the recovery property of the neuron. The parameters a , w_0 , v_0 , and $\gamma > 0$ may be considered as conductance properties and combinations of membrane reversal potentials (see [7]). The function $f(v)$ determines the outward membrane current at v . In the total input current I_{total} we distinguish two sources: an eventual injected current I , which will be taken as constant throughout the paper, and the synaptic input $I_{syn}(v)$. In the the synaptic input term, v_{syn} symbolizes the reversal potential and $g_{syn} > 0$ is the synaptic conductance. Finally, C is related to the cell membrane capacitance and is

assumed to be small and bounded, that is, $0 < C \ll 0.1$. In the numerical simulations, v_{syn} is considered to be the half point between $a/2$ and $(1+a)/2$ to mimic an excitatory synapse.

At a first instance, the synaptic conductance, g_{syn} , is considered to be constant, a fact that can be understood as the synaptic current $I_{syn}(v)$ being a representation of the mean field of the synaptic inputs. Moreover, since C is assumed to be small, the variables evolve with very different velocities and so system (1) can be considered a slow-fast dynamical system, where the variable v is the fast one and the variable w is the slow one.

As has been reported in previous studies (see [1] and [25]), system (1) presents different neuronal behaviors depending on the total amount of constant current that the neuron is receiving. In particular, for $g_{syn} = 0$, the authors show that there exist two boundary values I_1^0 and I_2^0 such that if $I_{total} \leq I_1^0$, the system presents low activity and the membrane potential tends to a silent state, that is, variable v tends to an equilibrium state with low value. Moreover, when $I_1^0 < I_{total} < I_2^0$, the system exhibits a unique isolated periodic orbit, i.e., a limit cycle, and so the neuron presents an oscillatory behavior corresponding to a regular firing. Otherwise, if $I_{total} \geq I_2^0$, the neuron tends to a steady high activity, that is, the variable v tends to an equilibrium state with high value, corresponding to a nerve block.

In the present paper, we show that this scenario also persists for $I_{total} = I - I_{syn}(v) = I - g_{syn}(v - v_{syn})$ with $g_{syn} \geq 0$. Since we are interested in the estimation of conductance g_{syn} in spiking regimes, we will focus on the region of the parameter space where the model presents a limit cycle crossing the two switching manifolds $v = a/2$ and $v = (1+a)/2$. Several approximations of the period T of the limit cycle, exhibited by the McKean model (1) with $g_{syn} = 0$, have been recently studied. In [8], the period T is computed numerically for different constant inputs I_{total} . In other works, such as [1], [7], and [24], the approximation of T has been carried out by considering the singular limit ($C = 0$) of the limit cycle, which consists of segments of orbits from both subsystems, the slow and the fast one. The approximation is then obtained from the total amount of flight times on the slow manifold. We note that this value coincides with the constant term of the power series expansion in C of the period T . More recently, in [10], the authors provide an approximate expression of the period T by taking advantage of the slow invariant manifolds for $0 < C \ll 1$. In this case, T is approximated by computing the flight time of the limit cycle in each lateral region, i.e., in $v < a/2$ and $v > (1+a)/2$, by reducing the flow to the slow manifold, and supposing that the flight time in the central band, i.e., in $a/2 < v < (1+a)/2$, is negligible.

In this paper, we compute an approximated expression, \hat{T} , of the period function, T , which provides two new contributions to the existing literature. The first one is that instead of approximating the flight time in the lateral regions by reducing the flow to the slow manifold, we compute the exact value of this flight time. The second one is that we consider the flight time in the central region to be nonnegligible. As we will show in subsection 3.2, numerical evidence supports the goodness of the approximated period function in the sense that the absolute error, $|T - \hat{T}|$, is $O(C^\alpha)$, with $\alpha \approx 0.88 < 1$.

This new approximation of the period function denoted by \hat{T} depends on the parameters of the model, and, in particular, on the synaptic conductance g_{syn} and the applied current I , i.e., $\hat{T}(g_{syn}, I)$. As we prove in this article, the dependence of \hat{T} on the synaptic conductance, g_{syn} , is nonlinear but seems to be monotonic for the range of input current values for which \hat{T} has sense, that is, for the input currents that drive the neuron to regularly spike. Hence, as a

consequence of the monotonicity, by knowing \hat{T} and the applied current I (i.e., knowing the $f - I$ curve), one would be able to compute g_{syn} by solving numerically a nonlinear equation having a unique solution and so estimate the steady synaptic conductance of the neuron, which is the goal of this paper.

We would like to note that even though some studies consider the synaptic conductances as a constant input, in real experiments synaptic conductances change over time, thus causing nonregular spiking. Indeed, we have a nonautonomous system which may have a very complicated dynamics. If the changes in conductances are relatively slow, then we may assume to be “riding” on a periodic orbit with a constant conductance during a certain time window. This fact suggests that each interspike interval, which corresponds to the time between two consecutive spikes, can be a good approximation of T for a specific constant value \tilde{g}_{syn} provided that $g_{syn}(t)$ has a slow variation. Hence, for each interspike interval we estimate a different steady conductance and so we obtain a time course estimation of \tilde{g}_{syn} , say, $\hat{g}_{syn}(t)$; see subsection 4.2.

Furthermore, when the rate of variation of $g_{syn}(t)$ is close to that of V , the estimation $\hat{g}_{syn}(t)$ can be improved by taking advantage of the splitting of \hat{T} into subperiods accounting for the flight times in the lateral and the central regions; see subsection 4.3.

The above explained procedure and the results obtained in this article are distributed in the following way. In section 2, we present the model and revise the main features of its qualitative dynamics, namely, the existence and character of equilibrium points, and the conditions on the parameters that ensure the existence of a limit cycle. In section 3, we present the expression \hat{T} that we obtain as an approximation of the period T , showing numerical evidence that \hat{T} is a monotonically decreasing function of the synaptic conductance g_{syn} . In section 4, we deal with the estimation procedure, where we are able to infer, in subsection 4.2, a steady synaptic conductance from the cell’s oscillatory activity; in subsection 4.1, we extend the results to a more realistic case, where we present a proof of concept to estimate the full time course of the conductance. The conclusions are presented in section 5.

2. Qualitative analysis of the model. Let us consider the modified McKean model given by system (1). This system is a nonsymmetric continuous piecewise linear system that it is defined in three different regions, where $\{(v, w) \in \mathbb{R}^2; v < a/2\}$ is the left region, $\{(v, w) \in \mathbb{R}^2; v > (1 + a)/2\}$ is the right region, and $\{(v, w) \in \mathbb{R}^2; a/2 \leq v \leq (1 + a)/2\}$ is the central (or middle) one. Throughout the paper we will use the symbols L , R , and M to refer to these regions, respectively.

Observe that system (1) is not globally differentiable but piecewise differentiable. Moreover, since parameter C is assumed to be small, system (1) is endowed with a slow-fast dynamics, being the membrane potential, v , the fast variable; meanwhile the auxiliary variable, w , is the slow one. Notice that the dynamics of system (1) is parameterized by the slow time.

The function $f(v)$ depends piecewise linearly on the parameter v , with different slopes according to the three different zones defined by the model. Therefore the v -nullcline is a piecewise linear function, whereas the w -nullcline is a straight line; see Figure 1.

On the other hand, the determinant and the trace of the model vary across the different regions. In the central region, the determinant is given by $d_M = (\gamma(g_{syn} - 1) + 1)/C$, whereas

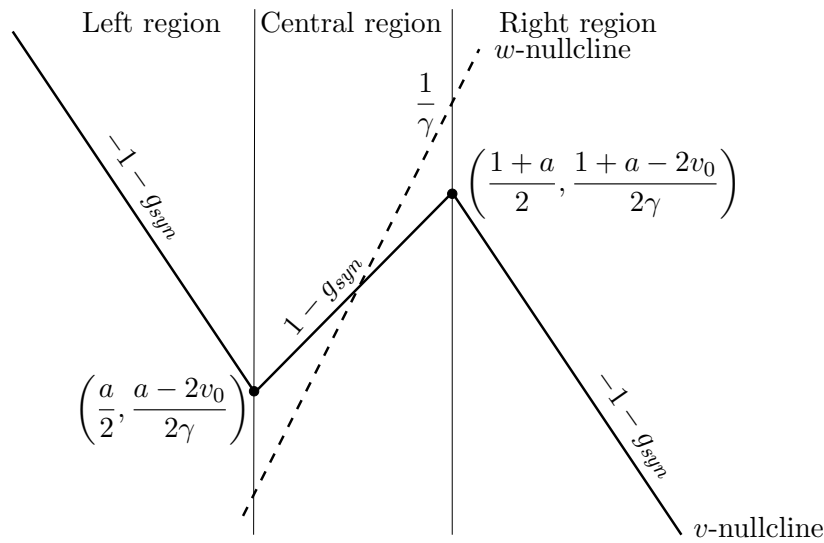


Figure 1. Representation of the v - and w -nullclines. The black dotted trace is the v -nullcline of system (1) and the black dashed trace is the w -nullcline. Filled circles describe the switching points, from one region to the other. The expression of the slopes of the nullclines as well as the coordinates of the switching points are also given in the figure.

the trace is $t_M = -((g_{syn} - 1)/C + \gamma)$. In the lateral regions, the determinants and traces are $d_L = d_R = (\gamma(1 + g_{syn}) + 1)/C$ and $t_L = t_R = -((1 + g_{syn})/C + \gamma)$, respectively, where the subscript L stands for the left region and R for the right one. As a consequence, different equilibrium points can coexist in the model and they can also be located in different regions. These facts depend on the value of the external input I and the synaptic conductance g_{syn} , as illustrated in Figure 2, where I_1 and I_2 are defined as

$$(2) \quad \begin{aligned} I_1 &= \left(\frac{a}{2} - v_{syn}\right) g_{syn} + \frac{(\gamma + 1)a - 2v_0 + 2\gamma w_0}{2\gamma}, \\ I_2 &= \left(\frac{a + 1}{2} - v_{syn}\right) g_{syn} + \frac{(\gamma + 1)a - 2v_0 + 2\gamma w_0 - \gamma + 1}{2\gamma}. \end{aligned}$$

In fact, $I_j \equiv I_j(g_{syn}; v_{syn}, \gamma, a, v_0, w_0)$, $j = 1, 2$, but we will omit these dependencies to simplify the notation. Note that when $g_{syn} < 1 - 1/\gamma$, lines $I = I_1$ and $I = I_2$ are the subcritical saddle-node-like bifurcations, where two equilibrium points annihilate each other after they collide.

In the next proposition, we show necessary and sufficient conditions to ensure existence and uniqueness of an equilibrium point of system (1) located in the central region or on either of the two switching manifolds. We point out that, from the arguments used in the proof of this proposition, the rest of the possible locations and configurations of equilibrium points given in Figure 2 follow.

Proposition 2.1. *Let us consider system (1) satisfying that $g_{syn} > 1 - 1/\gamma$ and $I \in [I_1, I_2]$. Then, this system has a unique equilibrium point and it is located*

- (a) *in the interior of the central region if and only if $I_1 < I < I_2$;*

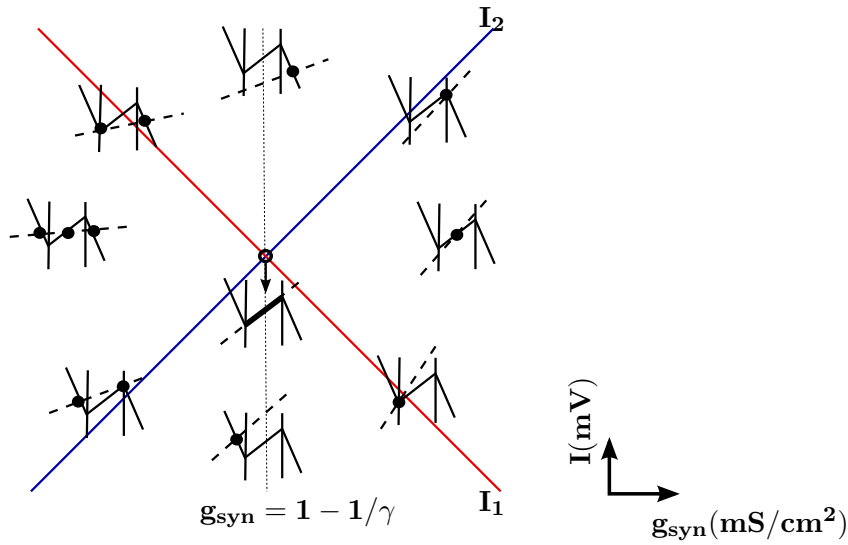


Figure 2. Location of the equilibrium points. According to expressions in (2), the solid blue line represents $I = I_2$, whereas the solid red line represents $I = I_1$. The dotted line is $g_{syn} = 1 - 1/\gamma$. Each picture in the figure represents the three different regions of system (1) (left, central, and right) separated by vertical segments. The solid piecewise line corresponds to the v -nullcline, whereas the dashed line stands for the w -nullcline. The dots on their intersection are the equilibrium points. The different locations and configurations of equilibria follow from Proposition 2.1 and from the arguments used in its proof.

- (b) on the switching manifold $v = a/2$ if and only if $I = I_1$;
- (c) on the switching manifold $v = (1 + a)/2$ if and only if $I = I_2$.

Proof. The equilibrium points of system (1) are given by the solutions of

$$(3) \quad -f(v) + \left(g_{syn} + \frac{1}{\gamma}\right)v = \frac{v_0}{\gamma} - w_0 + g_{syn}v_{syn} + I \quad \text{and} \quad w = \frac{v - v_0}{\gamma},$$

where $f(v)$ takes its expression according to the corresponding region. Therefore, we proceed by considering each of the regions separately.

Let us first consider the left region. Since $f(v) = -v$, $g_{syn} \geq 0$, and $\gamma > 0$, the unique solution of system (3) is given by the point $\mathbf{p}_L = (v_L, w_L)$, where

$$v_L = \frac{\gamma(I - w_0 + g_{syn}v_{syn}) + v_0}{1 + \gamma(1 + g_{syn})} \quad \text{and} \quad w_L = \frac{I - w_0 + g_{syn}(v_{syn} - v_0) - v_0}{1 + \gamma(1 + g_{syn})}.$$

Therefore, by imposing that $v_L < a/2$, it follows that \mathbf{p}_L is an equilibrium point in this region if and only if $I < I_1$.

In the central region, where $f(v) = v - a$, the unique solution of system (3) is the point $\mathbf{p}_M = (v_M, w_M)$ given by

$$v_M = \frac{\gamma(I - w_0 + g_{syn}v_{syn} - a) + v_0}{1 - \gamma(1 - g_{syn})} \quad \text{and} \quad w_M = \frac{I - w_0 + g_{syn}(v_{syn} - v_0) + v_0 - a}{1 - \gamma(1 - g_{syn})}.$$

Hence, by forcing v_M to lie in the interval $[a/2, (a + 1)/2]$, \mathbf{p}_M is an equilibrium point if and only if either of the pair of inequalities

$$g_{syn} > 1 - \frac{1}{\gamma} \quad \text{and} \quad I_1 \leq I \leq I_2 \quad \text{or} \quad g_{syn} < 1 - \frac{1}{\gamma} \quad \text{and} \quad I_2 \leq I \leq I_1$$

are held. However, notice that the first component of the equilibrium point is exactly $v = a/2$ when $I = I_1$, and so the equilibrium point is located in the left switching manifold. Similarly, when $I = I_2$, the equilibrium point is located in the right switching manifold. Otherwise, i.e., when $I_1 < I < I_2$, the equilibrium point stays inside the central region.

We remark that in the case where $g_{syn} = 1 - 1/\gamma$, if $I = I_1 = I_2$ all points along the central part of the v -nullcline are equilibrium points. This fact is caused by the slopes of v and w nullclines being the same.

Finally, in the right region, i.e., when $f(v) = 1 - v$, the unique solution of system (3) is the point $\mathbf{p}_R = (v_R, w_R)$ given by

$$v_R = \frac{\gamma(I - w_0 + g_{syn}v_{syn} + 1) + v_0}{1 + \gamma(1 + g_{syn})} \quad \text{and} \quad w_R = \frac{I - w_0 + g_{syn}(v_{syn} - v_0) - v_0 + 1}{1 + \gamma(1 + g_{syn})}.$$

Since $g_{syn} \geq 0$ and $\gamma > 0$, by imposing that $v_R > (1+a)/2$, an equilibrium point in this region exists if and only if $I > I_2$.

Hence, we only have an equilibrium point located in the central region when both conditions $g_{syn} > 1 - 1/\gamma$ and $I_1 \leq I \leq I_2$ hold, proving the proposition. \blacksquare

Remark 2.2. By Proposition 2.1, when $g_{syn} > 1 - 1/\gamma$ and $I_1 < I < I_2$ system (1) has only one equilibrium point which lies in the interior of the central region. Let us call such point $\mathbf{p}_M = (p_{v,M}, p_{w,M})$. When each linear system which is part of the vector field is considered to be defined on the full plane, then two more zeros appear: one from the system described in the left zone, $\mathbf{p}_L = (p_{v,L}, p_{w,L})$, and another from the system in the right zone, $\mathbf{p}_R = (p_{v,R}, p_{w,R})$. Under these assumptions, these two points are located in the central region and, even thinking that they have influence on the global dynamics, they are not equilibrium points of system (1). These points are called virtual equilibrium points. Finally, note that when $I = I_1$ or $I = I_2$, \mathbf{p}_M coincides with \mathbf{p}_L or \mathbf{p}_R , respectively.

Even though the full model is not linear, its behavior is locally governed by the eigenvalues associated with each one of the linear subsystems. Note that these eigenvalues vary across the three different zones (left, central, and right). In each region, there exist two different eigenvalues: one of $O(C^0)$, which is responsible for the slow dynamics and denoted by the subscript s , and another one of $O(C^{-1})$, which is responsible for the fast dynamics and is denoted by the subscript q . These eigenvalues are given by

$$\begin{aligned} \lambda_{s,L} = \lambda_{s,R} &= -\frac{1}{2C} \left(1 + g_{syn} + C\gamma - \sqrt{(1 + g_{syn} - C\gamma)^2 - 4C} \right), \\ \lambda_{q,L} = \lambda_{q,R} &= -\frac{1}{2C} \left(1 + g_{syn} + C\gamma + \sqrt{(1 + g_{syn} - C\gamma)^2 - 4C} \right), \\ \lambda_{s,M} &= \frac{1}{2C} \left(1 - g_{syn} - C\gamma - \sqrt{(g_{syn} - 1 - C\gamma)^2 - 4C} \right), \\ \lambda_{q,M} &= \frac{1}{2C} \left(1 - g_{syn} - C\gamma + \sqrt{(g_{syn} - 1 - C\gamma)^2 - 4C} \right). \end{aligned}$$

They may correspond to either focus or node equilibrium points, depending on the values of the parameters g_{syn} , γ , and C . However, for sufficiently small values of C , one can guarantee that all equilibrium points are nodes since all the discriminants are positive when $C = 0$. In fact, all the equilibrium points are nodes if and only if $C \leq C^*$, where

$$C^* = \min \left\{ \frac{2 + \gamma(g_{syn} + 1) - 2\sqrt{1 + \gamma(g_{syn} + 1)}}{\gamma^2}, \frac{2 + \gamma(g_{syn} - 1) - 2\sqrt{1 + \gamma(g_{syn} - 1)}}{\gamma^2} \right\}.$$

In this case, we call $\mathbf{v}_{i,j} = (\lambda_{i,j} + \gamma, 1)$ the eigenvector associated with the eigenvalue $\lambda_{i,j}$, where $i \in \{s, q\}$ and $j \in \{L, R, M\}$. Notice that the slow motion takes place along manifolds that are defined by the eigenvector associated with the slow eigenvalue. Since the eigenvector depends on the region, we obtain three different slow manifolds. We refer to each slow manifold as S_j , where $j \in \{L, R, M\}$, which are given by

$$\begin{aligned} (4) \quad S_L &= \left\{ (v, w); v < \frac{a}{2} \quad \text{and} \quad w = p_{w,L} + \frac{v - p_{v,L}}{\lambda_{s,L} + \gamma} \right\}, \\ S_R &= \left\{ (v, w); v > \frac{1+a}{2} \quad \text{and} \quad w = p_{w,R} + \frac{v - p_{v,R}}{\lambda_{s,R} + \gamma} \right\}, \\ S_M &= \left\{ (v, w); \frac{a}{2} \leq v \leq \frac{1+a}{2} \quad \text{and} \quad w = p_{w,M} + \frac{v - p_{v,M}}{\lambda_{s,M} + \gamma} \right\}, \end{aligned}$$

where $p_{v,j}$ and $p_{w,j}$ are the first and second components, respectively, of \mathbf{p}_j (see Remark 2.2).

Since the piecewise differential system (1) is locally linear, it can be analytically solved at each region separately, being the local solutions

$$(5) \quad \begin{pmatrix} v(t) \\ w(t) \end{pmatrix} = c_{1,i} e^{\lambda_{s,i} t} \mathbf{v}_{s,i} + c_{2,i} e^{\lambda_{q,i} t} \mathbf{v}_{q,i} + \mathbf{p}_i,$$

where i represents either L , M , or R depending on the region being left, central, or right, respectively, and

$$(6) \quad c_{1,i} = \frac{v(0) - p_{v,i} - (\lambda_{q,i} + \gamma)(w(0) - p_{w,i})}{\lambda_{s,i} - \lambda_{q,i}}, \quad c_{2,i} = w(0) - c_{1,i} - p_{w,i}.$$

Notice that (5) only represents a local expression of the solution of system (1). As long as the orbit, given by a fixed initial condition, remains in one region, this orbit is given by the expression of the solution of the system obtained in this particular region; however, if the orbit crosses to another region, the orbit is given by the corresponding expression obtained in this new region, which depends on the different eigenvalues and initial conditions. Since the vector field defined by system (1) is globally nonlinear, system (1) may exhibit limit cycles (see [16]). In the next proposition we give a sufficient condition so that system (1) can have a limit cycle.

Proposition 2.3. *Consider the following assumptions:*

$$g_{syn} > 1 - 1/\gamma, \quad |g_{syn} + C\gamma| < 1, \quad \text{and} \quad 0 < C \leq C^*.$$

Then,

- (a) if $I_1 < I < I_2$, system (1) exhibits a unique limit cycle, this orbit crosses the two switching manifolds $v = a/2$ and $v = (a + 1)/2$, and it is stable;
- (b) if $I = I_1$ or $I = I_2$, system (1) exhibits a homoclinic orbit to the equilibrium point \mathbf{p}_M , this orbit is stable from the exterior and delimits an open region which is foliated by homoclinic orbits to \mathbf{p}_M .

Proof. Let us consider system (1) written in its Liénard form. To do that, we make two different changes of variables. First, we switch to (v, u) through $w = C(u + \gamma v)$ and, second, we introduce (x, y) , where $x = 4v - 2a - 1$ and $Cy = 4Cu + C\gamma(2a + 1) - 4I + 2a - 1$ (see section 2 in [16]). Then, moving the origin to the point $(0, ((2a + 1 - yv_{syn})g_{syn} + 4w_0)/C)$, the Liénard form of system (1) is given by

$$\begin{cases} \dot{x} = F(x) - y, \\ \dot{y} = G(x) - \delta, \end{cases}$$

where $\delta = -\frac{1}{C}(2a(\gamma + \gamma g_{syn} + 1) - \gamma + \gamma g_{syn} + 1 - 4v_0 + 4\gamma(w_0 - I - g_{syn}v_{syn}))$,

$$F(x) = \begin{cases} t_L(x + 1) - t_M, & x < -1, \\ t_M x, & -1 \leq x \leq 1, \\ t_R(x - 1) + t_M, & x > 1, \end{cases} \text{ and } G(x) = \begin{cases} d_L(x + 1) - d_M, & x < -1, \\ d_M x, & -1 \leq x \leq 1, \\ d_R(x - 1) + d_M, & x > 1. \end{cases}$$

By Proposition 2.1, since $g_{syn} > 1 - 1/\gamma$ and $I_1 < I < I_2$, only one equilibrium point exists and it is located in the interior of the central region. Moreover, since $g_{syn} > 1 - 1/\gamma$ and $|g_{syn} + C\gamma| < 1$, the parameters of the functions $F(x)$ and $G(x)$ satisfy that $d_M > 0$, $-d_M < \delta < d_M$, $d_L, d_R \geq 0$, $t_L, t_R < 0$, and $t_M > 0$. Hence, the existence and uniqueness of a limit cycle (isolated periodic orbit) surrounding the equilibrium point is guaranteed by Theorem 1 in [16].

Finally, since $0 < C \leq C^*$ and $t_M > 0$, the equilibrium point is a repelling node. Consequently, the invariant lines defined by the eigenvectors force the limit cycle to cross the three regions, which ends the proof of statement (a).

In order to prove statement (b), let us consider the case where $I = I_1$. Then, let $\mathbf{q}_L = (v_L, w_L)$ and $\mathbf{q}_R = (v_R, w_R)$ be the intersection points of the left and right slow manifolds (see (4)) with the vertical lines $v = a/2$ and $v = (1 + a)/2$, respectively, and let $\mathbf{q}_R^{**} = (v_R^{**}, w_R^{**})$ be the intersection point of the w -nullcline with the vertical line $v = (1 + a)/2$; see Figure 3.

In this case, the equilibrium point, \mathbf{p}_M (that exists and is unique from Proposition 2.1), coincides with the virtual equilibrium point of the left region, \mathbf{p}_L . Since it is contained in the intersection of S_L and S_M , which are respectively stable and unstable manifolds, the equilibrium point is a saddle node and $\mathbf{q}_L = \mathbf{p}_L$. Moreover, taking into account that $I = I_1$,

$$\mathbf{q}_L = \left(\frac{a}{2}, \frac{a - 2v_0}{2\gamma} \right), \quad \mathbf{q}_R = \left(\frac{1 + a}{2}, p_{w,R} + \frac{1}{\lambda_{s,R} + \gamma} \left(\frac{1 + a}{2} - p_{v,R} \right) \right), \text{ and}$$

$$\mathbf{q}_R^{**} = \left(\frac{1 + a}{2}, \frac{1 + a - 2v_0}{2\gamma} \right).$$

Consider now the closed region delimited by the union of the line segments $L_i, i = 1 \dots 5$, defined as follows:

- (i) L_1 denotes the line segment bounded by \mathbf{q}_L and the intersection point of S_R with the line $w = w_L$, which we denote by $\mathbf{q}_{1,R}^*$;
- (ii) L_2 denotes the segment of S_R that is bounded by $\mathbf{q}_{1,R}^*$ and \mathbf{q}_R ;
- (iii) L_3 denotes the vertical line segment bounded by \mathbf{q}_R and \mathbf{q}_R^{**} ;
- (iv) L_4 denotes the line segment bounded by \mathbf{q}_R^{**} and the intersection point of S_L with the line $w = w_R^{**}$, which we denote by $\mathbf{q}_{1,L}^*$; and, finally,
- (v) L_5 denotes the segment of S_L that is bounded by $\mathbf{q}_{1,L}^*$ and \mathbf{q}_L .

Looking at the direction of the flow, one can see that the w -component of the flow in L_1 is given by $\dot{w} = v - a/2$, which is positive in the line segment under consideration, and so the flow positively crosses L_1 . Similarly, the w -component of the flow on L_4 is given by $\dot{w} = v - (1 + a)/2$, which is negative in the line segment under consideration, and so the flow positively crosses L_4 . On the other hand, segments L_2 and L_5 are contained in the slow manifolds S_R and S_L , respectively; this fact implies that both line segments are invariant under the flow. Finally, notice that the flow positively crosses the line $v = (1 + a)/2$ if and only if $\dot{v} > 0$, and so

$$w|_{v=(1+a)/2} > 1 - \frac{1+a}{2} - w_0 + I - g_{syn} \left(\frac{1+a}{2} - v_{syn} \right).$$

Straightforward calculations show that, for a sufficiently small C , both w_R and w_R^{**} are greater than $w|_{v=(1+a)/2}$, and so the flow crosses the line segment L_3 positively, showing that the closed region obtained by these five segments is a compact set invariant under the flow of system (1); see Figure 3 (left) for a representation of both the invariant region and the direction of the flow. By the Poincaré–Bendixson theorem (see, for instance, [14, Theorem 4.1]), if there exists a limit cycle in the entering compact set, then there must exist an equilibrium point in its interior. However, the unique equilibrium point lies on the boundary of the closed region. Therefore, there cannot be limit cycles in the interior of the compact set. Consequently, again by the Poincaré–Bendixson theorem, the unique α - and ω -limit sets are on the boundary of

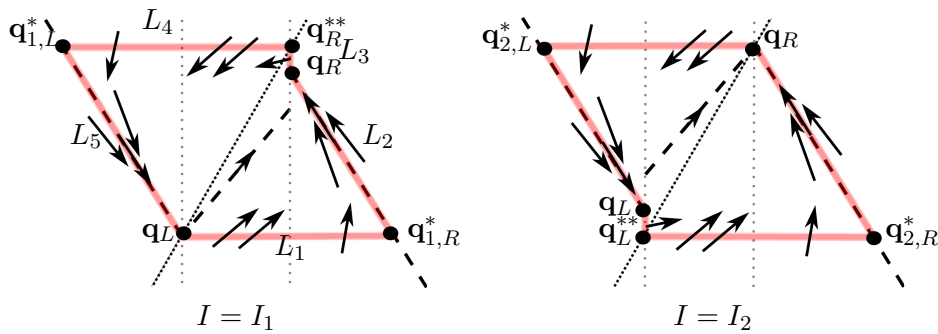


Figure 3. Invariant region and direction of the flow. Representation of the invariant regions and the direction of the flow when $I = I_1$ (left) and $I = I_2$ (right). The dashed black lines represent the three slow manifolds, whereas the dotted black line is the w -nullcline. Vertical dotted gray lines represent the two switching manifolds, $v = a/2$ (left line in each subplot) and $v = (1 + a)/2$ (right line in each subplot). The solid red line represents the boundary of each invariant region and the arrows give us information about the direction of the flow. See Proposition 2.3(b) for more details.

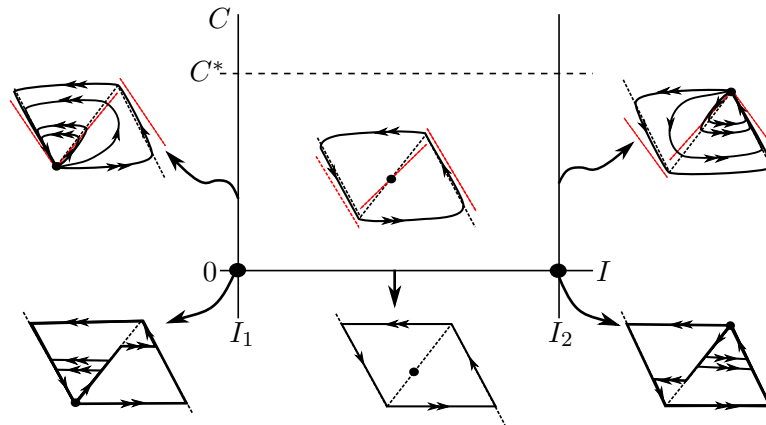


Figure 4. Bifurcation diagram. Representation of the bifurcation diagram with the phase portraits of the limit cycles for different values of C and I under conditions $g_{syn} > 1 - 1/\gamma$ and $|g_{syn} + C\gamma| < 1$. The phase portraits are obtained with the following parameter values: $a = 0.25$, $v_0 = 0$, $\gamma = 0.5$, $g_{syn} = 0.2$, $w_0 = 0$, and $v_{syn} = 1/4 + a/2$. The red dotted lines stand for the slow manifolds, whereas the dashed black lines stand for the v -nullcline.

the closed region. Hence, there exists a continuum of homoclinic orbits from the equilibrium point to itself, with the biggest homoclinic orbit stable. ■

Similar arguments can be applied to prove the result when $I = I_2$, where in this case $\mathbf{q}_R = \mathbf{p}_R$. In Figure 3 (right), we depict a representation of the invariant region and the directions of the flow in this case.

Remark 2.4. Note that under suitable conditions

$$(H) \quad g_{syn} > 1 - 1/\gamma, \quad |g_{syn} + C\gamma| < 1, \quad I_1 < I < I_2, \quad \text{and} \quad 0 < C \leq C^*,$$

the regular firing behavior persists for $g_{syn} \geq 0$.

Figure 4 represents the different phase portraits obtained when we change the value of the capacitance (when $C = 0$ and $0 < C \leq C^*$) and also the value of the applied current (when $I = I_1$, $I_1 < I < I_2$, and $I = I_2$). Notice that these configurations are obtained from Proposition 2.3.

3. Quantitative analysis of the limit cycle period. As mentioned in the introduction, related works such as [24] and [10], among others, make approximations of the period T of the limit cycle in system (1), where g_{syn} is considered to be identically zero. In this section we present a more accurate approximation of T , which also takes into account the case when g_{syn} is not identically zero. This improvement is, basically, obtained by considering the flight time in the central region and using a better approximation of the flight time in the lateral regions.

From now on, let us assume that the hypothesis (H) is satisfied. Hence, by Proposition 2.3(a), the considered model given by system (1) has a unique limit cycle that intercepts the three different regions, and so, the period of the limit cycle can be split into four parts: the first one corresponds to the time that the orbit is contained in the left region; the second

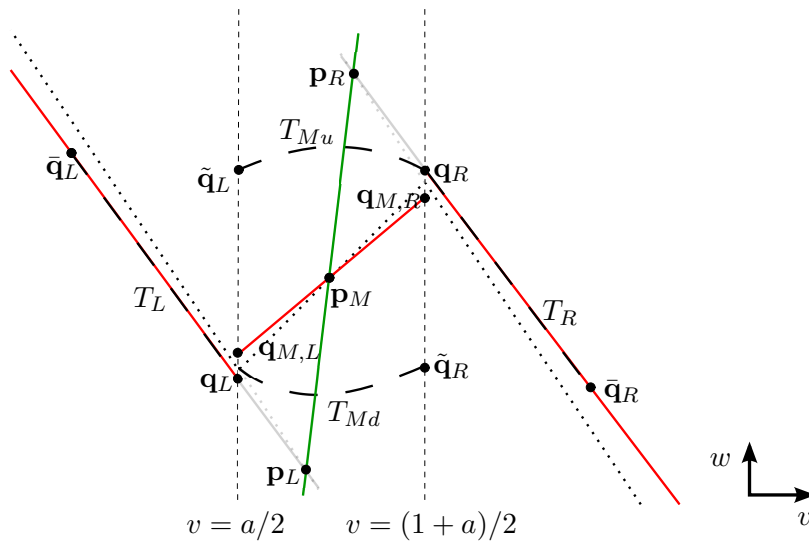


Figure 5. Key points when $C > 0$. Representation of all the elements needed to find the expression of the period. The vertical dashed black lines represent the boundaries of the different regions and the rest of the dashed black lines illustrate T_L , T_{Md} , T_R , and T_{Mu} . The dotted lines represent the critical manifold, whereas the red lines represent the three slow manifolds. These manifolds have been artificially prolonged in gray dotted lines and gray solid lines, respectively, for a better visualization of the virtual singular points. The green line stands for the w -nullcline. See the proof of Proposition 3.1 for more details.

part is the time taken by the orbit to cross the central zone from left to right following a counterclockwise movement; the third is the subperiod that the orbit lies in the right region; and, finally, the last part corresponds to the time taken by the orbit to cross the central part from right to left (see Figure 5). The total period, T , is then the sum of these four subperiods.

In the singular limit, that is, when $C = 0$, the limit cycle no longer exists. In fact, when C tends to zero, the limit cycle orbit tends to a limit set composed by two line segments on the critical manifold (slow subsystem) plus two more line segments on the stratified flow (fast subsystem); see Figure 4. We refer the reader to [21] for an overview on piecewise slow-fast dynamics terminology.

Comparing the flight time on the different segments, the one corresponding to the two line segments of the stratified flow can be considered zero with respect to the flight time on the two line segments of the critical manifold. Hence, we consider the flight time on the two line segments of the critical manifold, T_0 , as the limit of T when C tends to zero.

In the following subsections, we first provide an analytical expression approximating the period and then we computationally check the goodness of such approximation.

3.1. An approximation of the period of the limit cycle. In the following proposition we give an approximation, \hat{T} , of the total period. We also show that the singular limit of this expression results to be T_0 .

Proposition 3.1. *Given system (1) under hypothesis (H),*

- (a) *if $C = 0$, the flight time on the two line segments of the critical manifold is $T_0 = T_{0,L} + T_{0,R}$ such that*

$$(7) \quad T_{0,L} = B_0 \ln \left(\frac{\gamma(I - I_1)}{\gamma(I - I_1) + K_0} \right) \quad \text{and} \quad T_{0,R} = B_0 \ln \left(\frac{\gamma(I - I_2)}{\gamma(I - I_2) - K_0} \right),$$

$$B_0 = -\frac{1 + g_{syn}}{(1 + \gamma + \gamma g_{syn})}, \quad K_0 = \frac{(1 - g_{syn})(1 + \gamma + \gamma g_{syn})}{2(1 + g_{syn})};$$

(b) for a sufficiently small $C > 0$, the period of the unique limit cycle orbit of the system can be analytically approximated by $\hat{T} = T_L + T_{Mu} + T_{Md} + T_R$, where

$$(8) \quad T_L = \frac{1}{\lambda_{s,L}} \ln \left(\left| \frac{\gamma(I - I_1)}{\gamma(I - I_1) - K_l} \right| \right), \quad T_{Md} = \frac{1}{\lambda_{q,M}} \ln \left(\left| \frac{\gamma(I - I_2) + K_m}{\gamma(I - I_2) + K_{m,d}} \right| \right),$$

$$T_R = \frac{1}{\lambda_{s,L}} \ln \left(\left| \frac{\gamma(I - I_2)}{\gamma(I - I_2) + K_l} \right| \right), \quad T_{Mu} = \frac{1}{\lambda_{q,M}} \ln \left(\left| \frac{\gamma(I - I_1) + K_m}{\gamma(I - I_1) + K_{m,u}} \right| \right),$$

where

$$K_l = \frac{\gamma + \lambda_{q,L}}{2(\lambda_{q,L} - \lambda_{s,L})} (g_{syn}\gamma + \gamma + 2\lambda_{s,L} + 1),$$

$$K_m = \frac{(\gamma + \lambda_{s,M})(g_{syn}\gamma - \gamma + 1)((g_{syn}\gamma + 1)(\lambda_{s,L} - \lambda_{q,M}) - \gamma(\lambda_{s,L} + \lambda_{q,M}) - 2\lambda_{s,L}\lambda_{q,M})}{2(\gamma + \lambda_{q,M})((g_{syn}\gamma + 1)(\lambda_{s,L} - \lambda_{s,M}) - \gamma(\lambda_{s,L} + \lambda_{s,M}) - 2\lambda_{s,L}\lambda_{s,M})},$$

$$K_{m,d} = \frac{(\lambda_{q,M} - \lambda_{s,M})(\gamma + \lambda_{q,M})(g_{syn}\gamma - \gamma + 1)(g_{syn}\gamma + \gamma + 2\lambda_{s,L} + 1)}{2(\gamma + \lambda_{q,M})((g_{syn}\gamma + 1)(\lambda_{s,L} - \lambda_{s,M}) - \gamma(\lambda_{s,L} + \lambda_{s,M}) - 2\lambda_{s,L}\lambda_{s,M})},$$

$$K_{m,u} = \frac{(\gamma + \lambda_{q,M})(g_{syn}\gamma - \gamma + 1)((g_{syn}\gamma + 1)(\lambda_{s,L} - \lambda_{s,M}) - \gamma(\lambda_{s,L} + \lambda_{s,M}) - 2\lambda_{s,L}\lambda_{s,M})}{2(\gamma + \lambda_{q,M})((g_{syn}\gamma + 1)(\lambda_{s,L} - \lambda_{s,M}) - \gamma(\lambda_{s,L} + \lambda_{s,M}) - 2\lambda_{s,L}\lambda_{s,M})}.$$

Proof. Let us consider first the singular case when $C = 0$. In this case, since the left term of the first equation of system (1) vanishes, v can be isolated and replaced in the second equation of system (1), obtaining the following nonautonomous linear ordinary differential equations:

$$(9) \quad \begin{aligned} \dot{w} &= -(1 + \gamma)w - w_0 - v_0 + I - I_{syn} & \text{if } v < a/2; \\ \dot{w} &= -(1 + \gamma)w - w_0 - v_0 + I - I_{syn} + 1 & \text{if } v > (1 + a)/2. \end{aligned}$$

From this system, the flight time on the two line segments of the critical manifold can be analytically obtained by integrating the \dot{w} equation at each lateral region separately. From the first differential equation in (9), which corresponds to the left region, integrating from $t = 0$ to $t = T_{0,L}$ we calculate the left flight time $T_{0,L}$, and, from the second differential equation, which corresponds to the right region, integrating from $t = 0$ to $t = T_{0,R}$, we calculate the right flight time $T_{0,R}$. Then, we obtain the expressions (7), which proves statement (a).

Consider now the perturbed case, that is, when $C > 0$ and small enough. In this situation, it is well-known that the limit cycle evolves exponentially close to the lateral slow manifolds when they intersect the switching manifolds; see [11]. The intersection point with the left (resp., right) switching manifold is called \mathbf{q}_L (resp., \mathbf{q}_R); see Figure 5. Therefore, different techniques from the ones used when $C = 0$ are required to find an approximated period.

Since the period can be split into four parts, we can approximate them separately. Let us first approximate the central subperiods, T_{Md} and T_{Mu} , defined as the bottom and upper subperiods, respectively. Let $\mathbf{q}_{M,L}$ and $\mathbf{q}_{M,R}$ be the intersection points of the central slow manifold with $v = a/2$ and $v = (1 + a)/2$, respectively (see Figure 5 for a representation of these points).

Since the distance between the slow and critical manifolds of system (1) is of $O(C)$ (see [21]), the distance between \mathbf{q}_L and $\mathbf{q}_{M,L}$ is also of $O(C)$. Moreover, the distance between \mathbf{q}_R and $\mathbf{q}_{M,R}$ is also of $O(C)$. In fact, notice that \mathbf{q}_L (resp., \mathbf{q}_R) tends to $\mathbf{q}_{M,L}$ (resp., $\mathbf{q}_{M,R}$) when C tends to zero. The limit cycle follows the left slow manifold very close to it and crosses from the left region to the central one at some point between \mathbf{q}_L and $\mathbf{q}_{M,L}$, exponentially close to \mathbf{q}_L . Similarly, the orbit moves very close to the right slow manifold and crosses from the right region to the central one at some point between \mathbf{q}_R and $\mathbf{q}_{M,R}$, also exponentially close to \mathbf{q}_R (see Figure 4). Hence, since C is close to 0, one can assume that the integral curve through \mathbf{q}_L , which is contained in the central region, will remain in a neighborhood of the limit cycle, and similarly for the integral curve through \mathbf{q}_R . Therefore, we consider \mathbf{q}_L and \mathbf{q}_R as an approximation of two points where the limit cycle passes through.

Then, consider the central solution of the system, which is given in (5) when $i = M$, with \mathbf{q}_L and \mathbf{q}_R as initial conditions. Since the fast eigenvalue $\lambda_{q,M}$ is $O(C^{-1})$, whereas the slow eigenvalue $\lambda_{s,M}$ is $O(C^0)$ and C is sufficiently small, one can suppose that $\lambda_{s,M} = 0$ and, consequently, find an expression of the subperiods T_{Md} and T_{Mu} . Indeed, under the previous assumptions on the initial conditions, the subperiod T_{Md} corresponds to the piece of orbit that begins at \mathbf{q}_L and ends on the boundary $v = (1 + a)/2$ at a point that we call $\tilde{\mathbf{q}}_R$. By imposing that $v(t) = (1 + a)/2$ and $\lambda_{s,i} = 0$ in the first component of (5) when $i = M$, the subperiod T_{Md} is the result of isolating the time t . That is,

$$T_{Md} = \frac{1}{\lambda_{q,M}} \ln \left(\left| \frac{\gamma(I - I_2) + K_m}{\gamma(I - I_2) + K_{m,d}} \right| \right),$$

where K_m and $K_{m,d}$ are given in the statement of this proposition.

Similarly, the subperiod T_{Mu} corresponds to the piece of orbit that begins at \mathbf{q}_R and ends on the boundary $v = a/2$ at a point that we call $\tilde{\mathbf{q}}_L$. Therefore, following the same procedure as for T_{Md} , we obtain that

$$T_{Mu} = \frac{1}{\lambda_{q,M}} \ln \left(\left| \frac{\gamma(I - I_1) + K_m}{\gamma(I - I_1) + K_{m,u}} \right| \right),$$

where $K_{m,u}$ is described in the statement of this proposition.

Notice that both points $\tilde{\mathbf{q}}_R$ and $\tilde{\mathbf{q}}_L$ can be analytically computed by using the second coordinate of (5), since T_{Md} and T_{Mu} are known, and the component v of $\tilde{\mathbf{q}}_R$ and $\tilde{\mathbf{q}}_L$ is $v = (1 + a)/2$ and $v = a/2$, respectively. Then, the approximated period on the lateral regions will be the necessary time to travel from $\tilde{\mathbf{q}}_L$ to \mathbf{q}_L for the left subperiod, T_L , and the necessary time to travel from $\tilde{\mathbf{q}}_R$ to \mathbf{q}_R for the right subperiod, T_R .

Let us consider the coordinate system centered at the virtual equilibrium point \mathbf{p}_L and generated by the left eigenvectors $\mathbf{v}_{s,L}$ and $\mathbf{v}_{q,L}$. In this coordinate system $\tilde{\mathbf{q}}_L = \mathbf{p}_L + \bar{c}_1 \mathbf{v}_{s,L} + \bar{c}_2 \mathbf{v}_{q,L}$ and $\mathbf{q}_L = \mathbf{p}_L + c_1 \mathbf{v}_{s,L}$. Let $\bar{\mathbf{q}}_L = \mathbf{p}_L + \bar{c}_1 \mathbf{v}_{s,L}$ be the projection of $\tilde{\mathbf{q}}_L$ on the slow manifold along the direction given by the fast eigenvector $\mathbf{v}_{q,L}$.

The time T_L is computed as the time spent by the limit cycle to go from $\bar{\mathbf{q}}_L$ to \mathbf{q}_L . See Figure 5 for a representation. Then, by isolating t in expression

$$e^{t\lambda_{s,L}}\bar{c}_1\|\mathbf{v}_{s,L}\| = c_1\|\mathbf{v}_{s,L}\|,$$

we obtain

$$T_L = \frac{1}{\lambda_{s,L}} \ln \frac{c_1}{\bar{c}_1}.$$

The expressions of c_1 and \bar{c}_1 can be easily obtained from expression (6).

The expression of T_R can be similarly computed by considering the expression of the points \mathbf{q}_R and $\bar{\mathbf{q}}_R$ in the coordinate system centered at the virtual equilibrium point \mathbf{p}_R and generated by the right eigenvectors $\mathbf{v}_{s,R}$ and $\mathbf{v}_{q,R}$.

Therefore, an expression approximating the period of the limit cycle in system (1) is $\hat{T} = T_L + T_{Md} + T_R + T_{Mu}$, thus proving statement (b). ■

Remark 3.2. Note that since $\bar{\mathbf{q}}_L$ is the projection of $\tilde{\mathbf{q}}_L$ on the slow manifold along the direction given by the fast eigenvector $\mathbf{v}_{q,L}$ and system (1) is linear in the left region, the subperiod T_L is the flight time between $\tilde{\mathbf{q}}_L$ and \mathbf{q}_L . Similarly, the subperiod T_R is the flight time between $\tilde{\mathbf{q}}_R$ and \mathbf{q}_R .

Remark 3.3. When C tends to 0, $T_L \rightarrow T_{0,L}$, $T_{Md} \rightarrow 0$, $T_R \rightarrow T_{0,R}$, and $T_{Mu} \rightarrow 0$. Therefore, $\hat{T} \rightarrow T_0$. Moreover, for both $C = 0$ and $C > 0$, the left subperiod tends to infinity when I tends to I_1 . This limit agrees with the fact that, when $I = I_1$, the equilibrium point lies on the intersection of the central slow manifold with the vertical line $v = a/2$; therefore, the orbit reaches the equilibrium point and spends infinite time to escape. Similar arguments explain why the right subperiod tends to infinity when I tends to I_2 .

Remark 3.4. Notice that K_l , K_m , $K_{m,d}$, and $K_{m,u}$ in the expression \hat{T} of Proposition 3.1 have a nonlinear dependence on g_{syn} . Moreover, fixing all parameters in the model but keeping the synaptic conductance, g_{syn} , the applied current, I , and the parameter related to the capacitance of the neuron, C , as variables, the approximated period can be written as the function

$$\hat{T}(C, I, g_{syn}) = T_L(C, I, g_{syn}) + T_{Md}(C, I, g_{syn}) + T_R(C, I, g_{syn}) + T_{Mu}(C, I, g_{syn}).$$

3.2. Goodness of the approximated period function. As mentioned in the proof of Proposition 3.1, in order to approximate the period, we have assumed that the points \mathbf{q}_L and \mathbf{q}_R belong to the limit cycle, because they are exponentially close to the orbit. To see the global effect that this assumption causes, and so the goodness of fit, in Figure 6 we show the relative error of the approximated period function $\hat{T}(C, I, g_{syn})$, first, keeping constant parameter g_{syn} (panel A); second, keeping constant capacitance C (panel B); and, finally, keeping constant applied current I (panel C). The relative errors have been plotted, in all panels, considering the numerical solution of the period, which has been computed using the Newton–Raphson method in each region separately, as well as the actual one (see Appendix B.1 for details on the routine). In panel A we can see how the relative error in the proposed approximation function depends more significantly on the capacitance C than on the applied

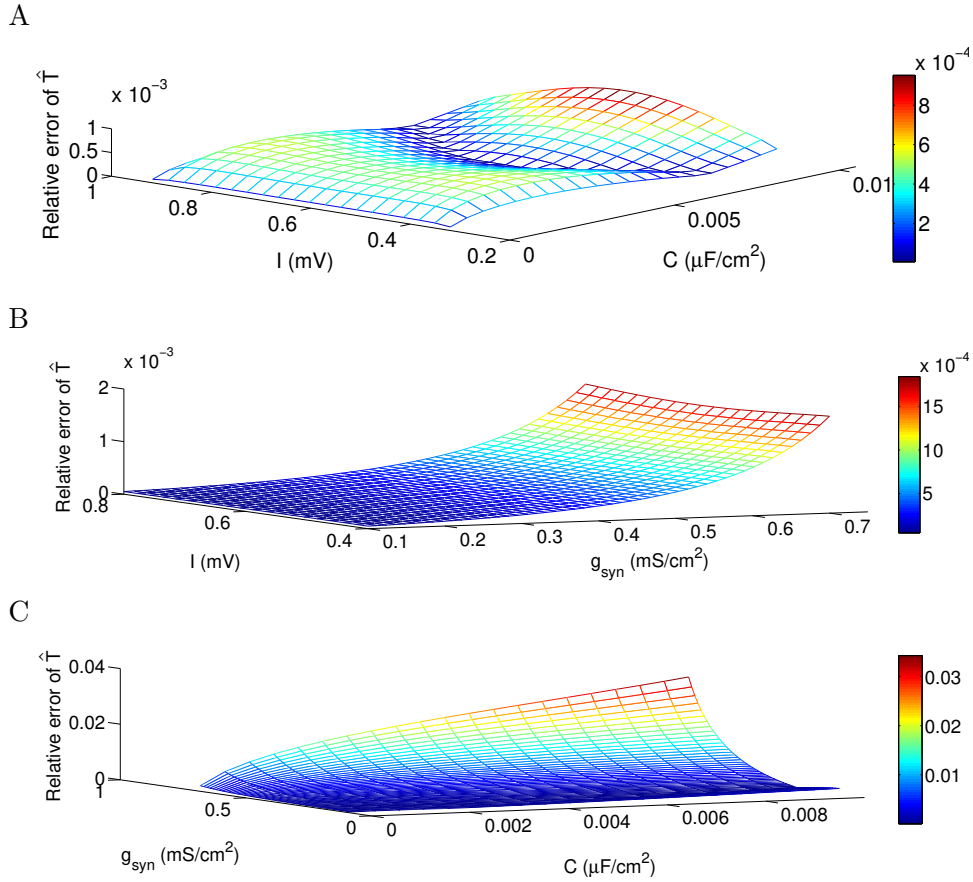


Figure 6. Goodness of fit of the periodic function $\hat{T}(C, I, g_{\text{syn}})$. Panel A shows the relative error of the period for a fixed synaptic conductance $g_{\text{syn}} = 0.2$, panel B shows the relative error of the period when the capacitance is fixed as $C = 1e-4$, and panel C shows the relative error of the period when the applied current is fixed as $I = (I_1^0 + I_2^0)/2$ such that I_1^0 and I_2^0 are, respectively, the value of I_1 and I_2 corresponding to $g_{\text{syn}} = 0$. Relative errors are obtained by comparing the expression of \hat{T} in Proposition 3.1 with the integration time, computed from the Poincaré map using the Newton–Raphson method. The rest of the parameters of the model are fixed as $a = 0.25$, $v_0 = 0$, $w_0 = 0$, $\gamma = 0.5$, and $v_{\text{syn}} = 0.25 + a/2$.

current I . On the other hand, in panel B, one can see that when parameter I varies, for a fixed value of g_{syn} , the error is not qualitatively altered, but for larger values of g_{syn} , the relative error significantly increases; see also panel C, where we can better appreciate the errors in g_{syn} as C changes.

Observe that even though $\hat{T}(C, I, g_{\text{syn}})$ is defined for all values of C , g_{syn} , and I , computing \hat{T} makes sense only under the hypothesis (H), that is, when I lies in (I_1, I_2) and $g_{\text{syn}} \in (1 - 1/\gamma, 1 - C\gamma)$. Later, Figure 8 shows the shape of the approximated period function $\hat{T}(C, I, g_{\text{syn}})$ in the corresponding domain. As mentioned in Remark 3.3, the period substantially increases when I is close to I_2 and I_1 , tending to infinity. Moreover, the V -shaped domain of the function $\hat{T}(C, I, g_{\text{syn}})$ is given by the linear dependence that I_1 and I_2 have on

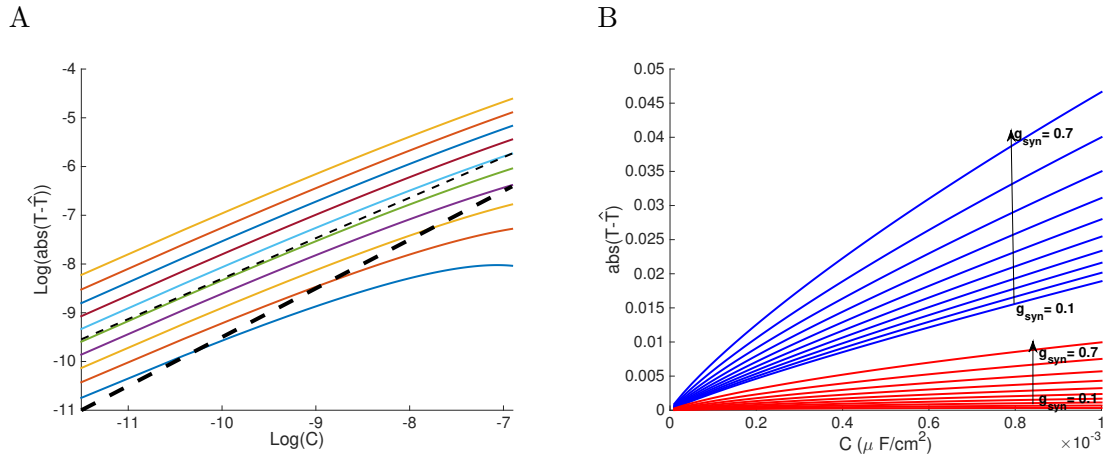


Figure 7. Asymptotic dependence of the absolute error with respect to C . Panel A shows the $\log(C)$ versus $\log(|T - \hat{T}|)$ for 10 equally spaced values of g_{syn} , moving from 0.1 (bottom colored trace) to 0.7 (upper colored trace). The black thick dashed trace stands for a line of slope 1, whereas the thin one stands for a line of slope 0.88. Panel B represents the error $|T - \hat{T}|$ (red traces) and the error obtained after avoiding the fast motion and reducing the flow to the slow manifold (blue traces) for the same different values of g_{syn} . In both panels, the applied current is fixed as $I = (I_1^0 + I_2^0)/2$ such that I_1^0 and I_2^0 are, respectively, the value of I_1 and I_2 corresponding to $g_{syn} = 0$. The rest of parameters of the model are fixed as $a = 0.25$, $v_0 = 0$, $w_0 = 0$, $\gamma = 0.5$, and $v_{syn} = 0.25 + a/2$. The numerical period T has been obtained applying the Newton–Raphson method to the Poincaré map associated with the periodic orbit.

g_{syn} . That is, as we decrease the value of g_{syn} , the value of I_1 is greater, whereas the value of I_2 is smaller; consequently, the window where I can move decreases and causes the V -shaped profile.

In Figure 7 we illustrate the asymptotic dependence of the absolute error with respect to C , showing a good linear fit of $\log(|T - \hat{T}|)$ versus $\log(C)$. The slope of this linear fitting provides the order of the absolute error in terms of C . In panel A we can observe, for different values of g_{syn} , that all traces have an initial slope smaller than one (comparing colored lines versus the black thick dashed line) and similar to 0.88 (comparing colored lines versus the black thin dashed line). Hence, our estimation procedure gives an absolute error of $O(C^\alpha)$ with $\alpha \approx 0.88$. In panel B, we compare the error $|T - \hat{T}|$ with that obtained after avoiding the fast motion and reducing the flow to the slow manifold. We can see that our method reduces the absolute error for any value of g_{syn} .

Remark 3.5. In Figure 8 we can also see that $\hat{T}(C, I, g_{syn})$ seems to be monotonically decreasing with respect to g_{syn} . Because of the multitude of parameters in the model, we have not been able to give an analytical proof of the monotonicity of \hat{T} . However, computational evidence is given; see Figure 8 and Appendix A. Note that, by assuming monotonicity, for a given value T^* of the period, there exists a unique value g_{syn}^* such that $\hat{T}(C, I, g_{syn}^*) = T^*$. In order to avoid possible situations of loss of monotonicity, in the estimation procedure of g_{syn} we have implemented a control to ensure, under some tolerance value, that the derivative of \hat{T} never vanishes.

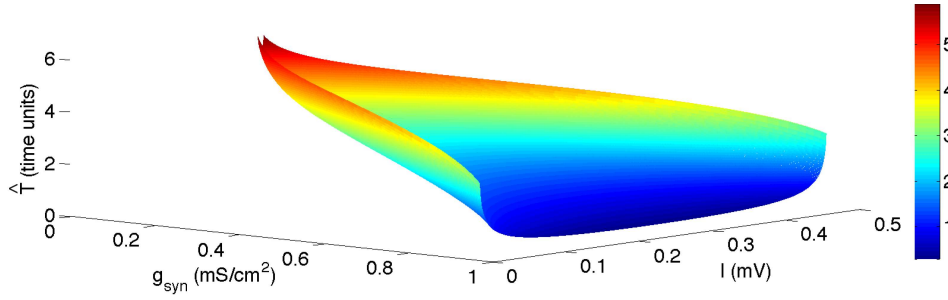


Figure 8. Shape of the $\hat{T}(C, I, g_{syn})$ function. This figure shows the shape of the approximated period \hat{T} versus the applied current I and the synaptic conductance g_{syn} . The capacitance has been fixed as $C = 1e - 4$. The rest of parameters of the model are fixed as $a = 0.25$, $v_0 = 0$, $w_0 = 0$, $\gamma = 0.5$, and $v_{syn} = 0.25 + a/2$.

4. Estimation of the synaptic conductance. In this section we present a method to estimate the steady synaptic conductance from the cell's oscillatory activity. That is, assuming that g_{syn} is constant and knowing the frequency of the spikes for a fixed and constant injected current I , we want to estimate the synaptic current that the neuron is receiving. The procedure will then be extended to estimate the time course of the nonsteady synaptic conductance.

4.1. Estimation of a steady synaptic conductance. Based on the evidence of the monotonicity of $\hat{T}(C, I, g_{syn})$ with respect to g_{syn} (see Figure 8 and Appendix A), we assume that there exists a one-to-one correspondence between \hat{T} and g_{syn} . Therefore, applying a specific current, I^* , one can experimentally approximate the corresponding actual period T^* of the membrane potential v , and so g_{syn} numerically. In other words, knowing the rest of the parameters of the model, a unique possible synaptic conductance g_{syn} can be estimated by solving the implicit equation

$$(10) \quad \hat{T}(C^*, I^*, g_{syn}) = T^*.$$

To solve equation (10), one has to take into account that the logarithmic part of the analytical expression \hat{T} contains an absolute function and, since I_1 and I_2 depend on g_{syn} , we could get up to three possible g_{syn} solutions for a fixed I . However, only one of the three possible solutions for g_{syn} satisfies that $I_1 < I < I_2$. Then, this indetermination can be removed by imposing the additional condition

$$(11) \quad g_{syn} > \max(0, \bar{I}_1, \bar{I}_2),$$

where

$$\bar{I}_1 = \frac{2\gamma I - (\gamma + 1)a + 2v_0 - 2\gamma w_0}{2\gamma(\frac{a}{2} - v_{syn})} \quad \text{and} \quad \bar{I}_2 = \frac{2\gamma I - (\gamma + 1)a + 2v_0 - 2\gamma w_0 - \gamma + 1}{2\gamma(\frac{a+1}{2} - v_{syn})}.$$

When we apply the estimation procedure (10)–(11) to obtain the estimated synaptic conductance, \hat{g}_{syn} , we identify two main sources of error: an error coming from the numerical method used to solve the implicit equation and another error coming from the approximation of the period function, which is at most $O(C^\alpha)$ with $\alpha \approx 0.88$ (see subsection 3.2). To

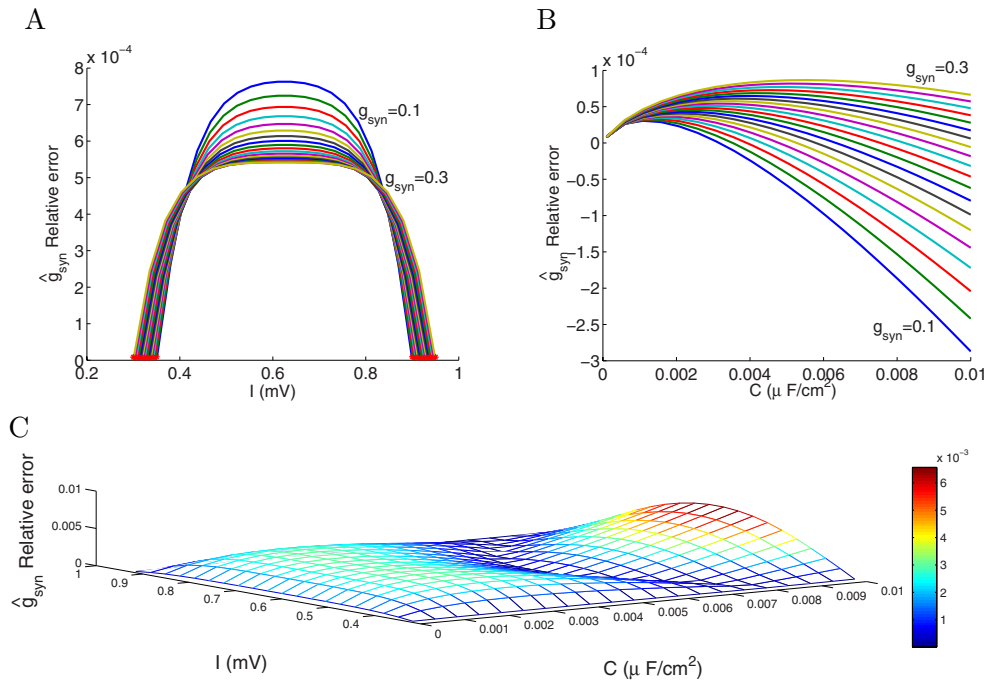


Figure 9. Goodness of fit of the steady synaptic conductance parameter. Panels A and B show the relative error caused when we estimate the synaptic conductance. The different traces correspond to different values of g_{syn} equally spaced from 0.1 to 0.3. Panel A represents the relative error versus the applied current for a fixed value of $C = 10^{-4}$, whereas panel B represents the relative error versus the membrane capacitance for a fixed value of $I = I_1 + 10^{-3}$. Red points in panel A represent the values of I_1 (left points) and I_2 (right points) for each g_{syn} . Panel C shows the relative error in absolute value for varying values of the membrane capacitance, C , and the applied current, I , being the actual synaptic conductance $g_{syn} = 0.2$. The rest of parameters are fixed as $a = 0.25$, $v_0 = 0$, $w_0 = 0$, $\gamma = 0.5$, and $v_{syn} = 0.25 + a/2$.

visualize the impact of both error sources and so to test the goodness of the estimation procedure, we show the relative error of the estimated synaptic conductance \hat{g}_{syn} with respect to the actual value of g_{syn} , both using different values of applied currents (see Figure 9(A)) and using different values of the membrane capacitance (see Figure 9(B)). In these plots we estimate different values of the synaptic conductance (from 0.1 to 0.3, equally spaced), each one represented by a different color trace.

In Figure 9(A) we can see how the estimation of the conductance improves when the applied current is close to I_1 and I_2 . The error of \hat{g}_{syn} takes its maximum at $I = (I_1 + I_2)/2$, where the slope of $\hat{T}(I)$ is minimal (in absolute value). On the other hand, in Figure 9(B) we also observe that the relative error is smaller when the membrane capacitance, C , is smaller; moreover, for small C one can appreciate that this error is notably less than $O(C^\alpha)$ with $\alpha \approx 0.88$. Therefore, we can conclude that the best estimation is done for small values of C and also for values of I close to I_1 or I_2 . In Figure 9(C) we can better appreciate how the error increases for large values of C and for values of I far from I_1 and I_2 . This panel presents the goodness of fit of the synaptic conductance when both parameters C and I change (in this plot, the relative error is represented in absolute value).

4.2. Generalization for nonconstant conductance's traces: Interspike estimation.

In this section, we modify the previous methodology in order to estimate conductance's traces that slowly vary along time, that is, when $g_{syn} = g_{syn}(t)$. Strictly speaking, this leads to a nonautonomous differential system, and the system may not have a limit cycle as for constant g_{syn} . However, for slow changes in the synaptic conductance, even if the limit cycle does not persist, we may assume that the orbits of the system are close to an oscillatory behavior. Given an interspike interval $[t^*, t^* + \tau]$, we propose to apply the associated procedure (10)–(11), that is, solving $\hat{T}(g_{syn}) = \tau$ to obtain an estimated \hat{g}_{syn} on $[t^*, t^* + \tau]$. We summarize this idea in the following procedure.

Method 4.1. Consider a voltage trace $\{v(t), t \in [0, T_{max}]\}$ obtained from the neuron model (1) under an (unknown) synaptic input $\{g_{syn}(t), t \in [0, T_{max}]\}$ and a specific applied current I^* such that they induce spiking activity. We assume that $v(t)$ reaches $N + 1$ peaks (maxima of the trace) and call $\{T^{(k)}\}_{k=1}^N$ the corresponding N interspike intervals. Then, the time course of the synaptic conductance $g_{syn}(t)$ can be estimated with the next steps:

1. For each $T^{(k)}$, $k = 1, \dots, N$, solve system (10)–(11) to estimate the corresponding synaptic conductance value, $\hat{g}_{syn}^{(k)}$.
2. Assign at $\hat{g}_{syn}^{(k)}$ the time $t^{(k)}$ corresponding to the $(k + 1)$ th peak to obtain a set of points $\mathcal{P} := \{(t^{(k)}, \hat{g}_{syn}^{(k)})\}_{k=1}^N$.

As a result of this procedure, we obtain a discrete series of \hat{g}_{syn} values, which are finally interpolated to obtain an approximation of the full time course of $\hat{g}_{syn}(t)$. In the forthcoming examples, we have used cubic spline interpolation. Notice also that we arbitrarily set $t^{(k)}$ as the last time in the corresponding interval; we have tested other choices (e.g., the middle point) and no substantial changes have been observed.

Figure 10 shows some test conductance's traces which have been created in order to obtain scenarios with different spiking intensities. The first two rows present conductance's traces with low frequency oscillations at different phases: the first one presents high amplitude oscillations, $g_{syn}(t) = 0.2 + 0.2 \sin(2\pi t/10)$, and the second one combines small with big oscillations, $g_{syn}(t) = 0.2 + 0.2 \sin(2\pi t/10) + 0.04 \sin(2\pi t/5)$. In both cases we obtain a good estimation of the conductance, according to the high concentration of points on the vicinity of the identity line in the scatter plots; see the panels in the second column of Figure 10. The reconstruction of membrane potential ($v_{rec}(t)$) obtained using the estimated conductance's trace $\hat{g}_{syn}(t)$ as synaptic input show an excellent agreement with the original membrane potential trace; see the panels in the last column.

In the last row of Figure 10, we consider a new conductance's trace where both frequency and amplitude of the small oscillations have been changed with respect to the results in the second row, $g_{syn}(t) = 0.4 + 0.2 \sin(2\pi t/2) + 0.1 \sin(2\pi t/20)$. In the left panel we can observe that the estimated conductance does not match with the actual ones, where the fast oscillations have not been captured. However, on the reconstruction of the membrane potential (see $v_{rec}(t)$ in the right panel on the last row), the frequency is captured, the amplitude of the spikes is not, and a small delay is presented.

From Figure 10, we conclude that for a slowly varying synaptic conductance, the method proposed in Method 4.1 gives estimates of the time course of the synaptic conductance

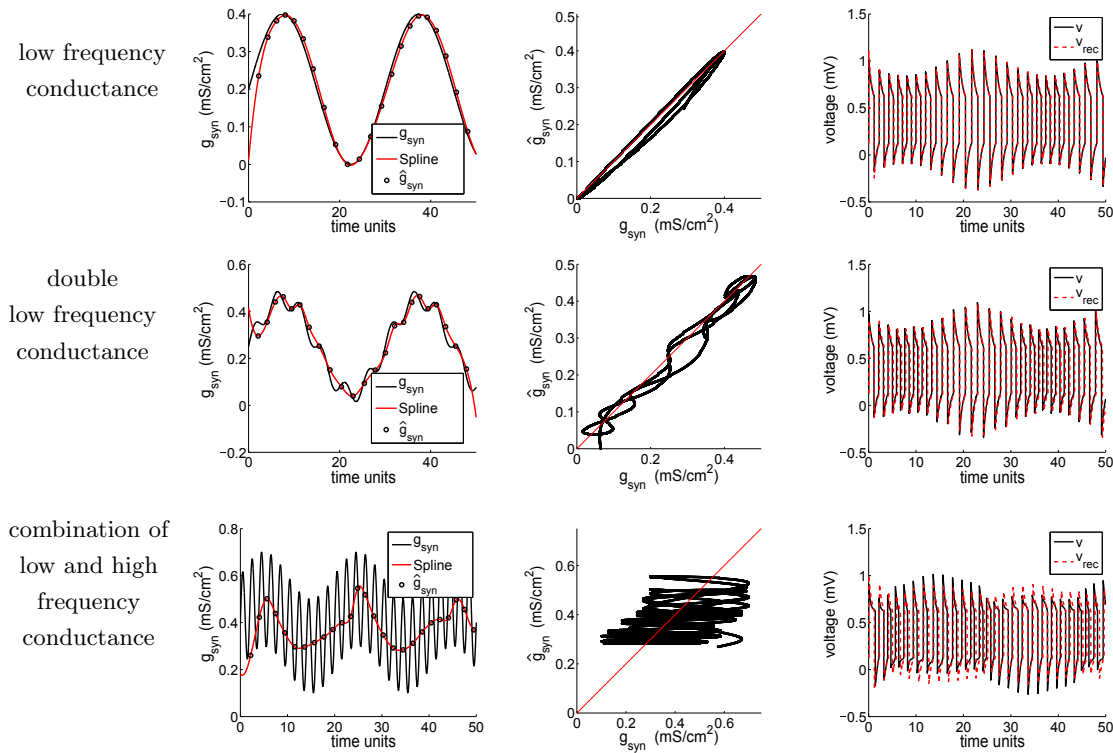


Figure 10. Goodness of fit of the synaptic conductance time course for different functions of g_{syn} . The first column shows the estimated values of the discretization of g_{syn} (black dots) and the cubic spline interpolation of them (red solid line). The black line corresponds to the actual value of the synaptic conductance at each time. The second column represents the scatter plot of the actual versus the estimated synaptic conductance after the interpolation. The red line is the identity line as a reference to observe the goodness of the estimation. The third column shows a comparison of the voltages computed using the actual conductance (solid black trace) and the estimated conductance (dotted red trace). Parameters are $a = 0.25$, $v_0 = 0$, $\gamma = 0.5$, $w_0 = 0$, $v_{\text{syn}} = 0.25 + a/2$, $C = 0.001 \mu\text{F}/\text{cm}^2$, and $I = 0.625 \mu\text{A}/\text{cm}^2$.

with small errors and reproducing the membrane potential with high accuracy. However, confronted to abrupt changes, the performance of the method weakens and can only track the mean time course of synaptic conductance, whereas the membrane potential is still well reconstructed.

To test the estimation of the conductance's course in a more realistic case, in Figure 11, we use 1 ms conductance's traces obtained from a computational network that models layer 4C α of primary visual cortex (see [18] and [23]). Panel A shows how the estimated conductance follows the trace of the actual ones but, as we can also see in Figure 10, higher oscillations are not well captured. We can corroborate this fact in panel B, where we show that the actual and estimated conductance are poorly correlated (the coefficient of correlation is approximately 0.12). In panel C we compare the voltage computed using the actual conductance's traces and the estimated ones (after interpolation). One can appreciate a small time shift of order 0.1 ms that remains almost constant along the time sequence.

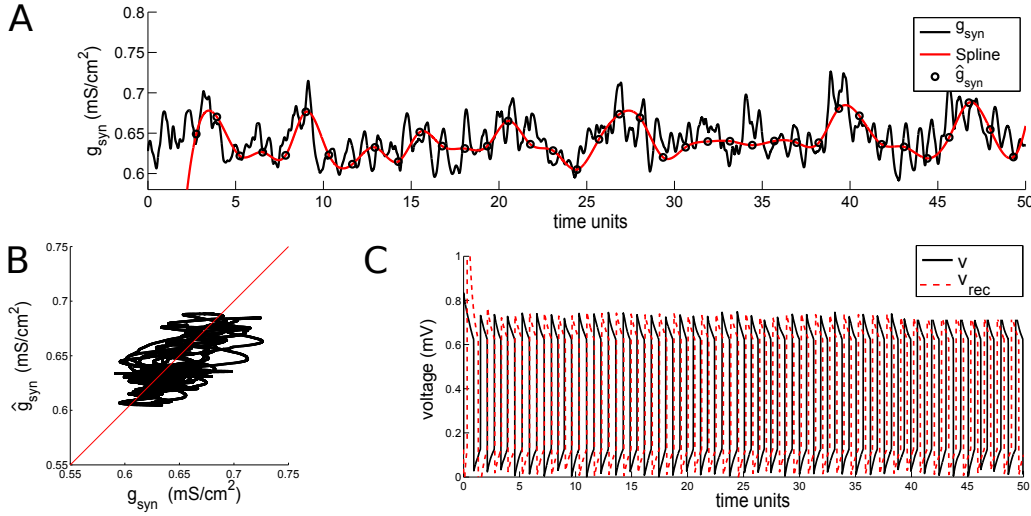


Figure 11. Goodness of fit of the time course of synaptic conductance based on interspike intervals. Panel A shows the estimated values of the discretization of g_{syn} (black dots) and the cubic spline interpolation of them (red solid line). The black line corresponds to the actual trace of synaptic conductance. Panel B represents the scatter plot of the actual versus the estimated synaptic conductance after the interpolation. The red line in panel B is the identity line, left as a reference to observe the goodness of the estimation. Panel C shows a comparison of the voltages computed using the actual conductance (solid black trace) and the estimated conductance (dotted red trace). Parameters are $a = 0.25$, $v_0 = 0$, $\gamma = 0.5$, $w_0 = 0$, $v_{syn} = 0.25 + a/2$, $C = 0.001 \mu F/cm^2$, and $I = 0.625 \mu A/cm^2$.

4.3. Generalization for nonconstant conductance's traces: Estimation based on the subperiods. In the previous section we have seen that for quickly varying conductance, we cannot obtain good estimations. These misestimations are partly due to the fact that we are assuming the conductance to be stationary in a quite long time window. To reduce the errors and to better capture the oscillations of the synaptic conductance, in this section we present a more accurate way to estimate $g_{syn}(t)$ by taking advantage of the approximated expression of each subperiod (the time spent in each region) separately in terms of g_{syn} , obtained in the proof of Proposition 3.1(b). We denoted these subperiods as T_L , T_{Mu} , T_{Md} , T_R . Similarly, for any monodromic trajectory of system (1), not necessarily periodic, we can split the trajectories into pieces lying on only one of the three regions. We denote by τ_ξ the time spent in region ξ to go from $v_{\xi,1}$ to $v_{\xi,2}$, where ξ stands for L , Md , Mu , or R , and the crossing points $v_{L,1} = v_{L,2} = v_{Md,1} = v_{Mu,2} = a/2$, $v_{R,1} = v_{R,2} = v_{Md,2} = v_{Mu,1} = (1+a)/2$. We understand that regions Mu and Md are both the central region. With this notation, we present a refined version of the estimation procedure given in Method 4.1.

Method 4.2. Consider a voltage trace $\{v(t), t \in [0, T_{max}]\}$ obtained from the neuron model (1) under an (unknown) synaptic input $\{g_{syn}(t), t \in [0, T_{max}]\}$ and a specific applied current I^* such that they induce spiking activity. We assume that the voltage trace describes N oscillations in the time interval $[0, T_{max}]$ and we define $\{\tau_\xi^{(k)}\}_{k=1}^N$ as the time spent to go from $v = v_{\xi,1}$ to $v = v_{\xi,2}$ in the k th oscillation, where ξ stands for L , Md , Mu , or R . Then, the time course of the synaptic conductance $g_{syn}(t)$ can be estimated by following the next steps:

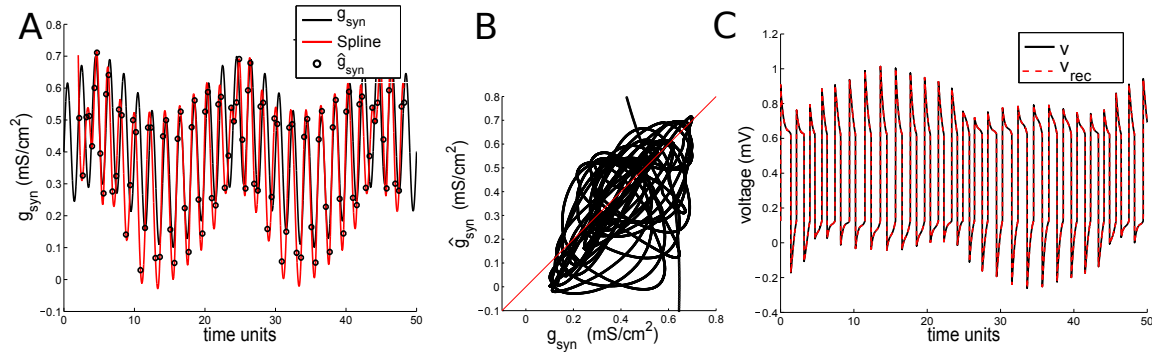


Figure 12. Goodness of fit of the synaptic conductance time course for the combination of low and high frequency conductance. Panel A shows the estimated values of the discretization of g_{syn} (black dots) and the cubic spline interpolation of them (red solid line). The black line corresponds to the actual value of the synaptic conductance at each time. Panel B represents the scatter plot of the actual versus the estimated synaptic conductance after the interpolation. The red line is the identity line as a reference to observe the goodness of the estimation. Panel C shows a comparison of the voltages computed using the actual conductance (solid black trace) and the estimated ones (dotted red trace). The other parameter values are $a = 0.25$, $v_0 = 0$, $\gamma = 0.5$, $w_0 = 0$, $v_{syn} = 0.25 + a/2$, $C = 0.001 \mu F/cm^2$, and $I = 0.625 \mu A/cm^2$.

1. For each $k = 1, \dots, N$ and $\xi \in \{L, Md, Mu, R\}$, solve

$$T_{\xi}(C^*, I^*, g_{syn}) = \tau_{\xi}^{(k)}$$

in terms of g_{syn} , under the constraint (11), and call the solution $\hat{g}_{syn}^{\xi,k}$.

2. Define the set $\mathcal{P} = \{(t^{\xi,k}, \hat{g}_{syn}^{\xi,k}); \xi = L, Md, Mu, R, k = 1, \dots, N\}$, where $t^{\xi,k}$ is the time when the k th oscillation crosses $v = v_{\xi,2}$.

As for Method 4.1, we finally interpolate the points of \mathcal{P} to obtain an approximation of the full time course of $\hat{g}_{syn}(t)$. Note that using Method 4.2 we can extract a more accurate discretization of the conductance's trace, as we can see in Figures 12 and 13. If we compare the results from those obtained by using Method 4.1, for instance, comparing the last row of Figure 10 to Figure 12, we observe how all the oscillations of $g_{syn}(t)$ are captured both in frequency and amplitude; concerning the reconstructed voltage in panel C, note that the delay detected when using Method 4.1 has been washed out with Method 4.2. For *in silico* data (see Figure 11(A) and Figure 13(A)), we can also appreciate an improvement of the estimation when using Method 4.2 even though the improvement is more evident when conductance changes abruptly. Hence, using Method 4.2 we can capture more oscillations.

When we apply Method 4.2 to the data obtained from the more realistic input to a single cell in the visual cortex (see Figure 13), the agreement between $g_{syn}(t)$ and $\hat{g}_{syn}(t)$ improves notably. This fact is reflected more clearly in panel A (compared to the same panel in Figure 11) rather than in the scatter plot of panel B, where it is difficult to tell a higher concentration of points around the identity line. Even though in this case the synaptic conductance is not perfectly estimated through time, we do capture the accurate mean conductance ($\text{mean}(g_{syn}) = 0.6350$ and $\text{mean}(\hat{g}_{syn}) = 0.6381$).

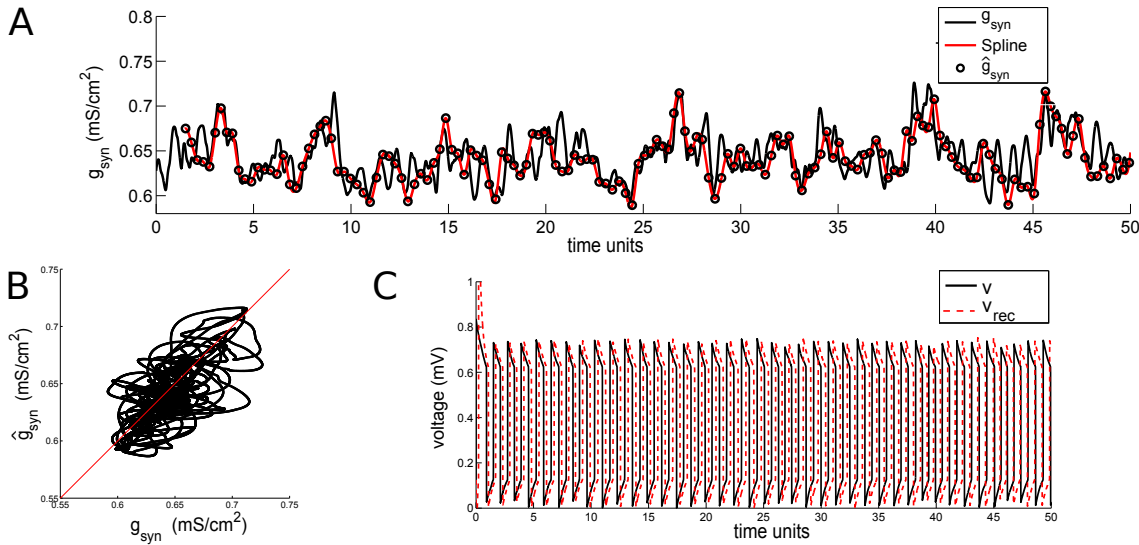


Figure 13. Goodness of fit of the synaptic conductance time course when we consider the subperiods separately. Panel A shows the cubic spline interpolation of the estimated values of the discretization of $g_{\text{syn}}(t)$ (red solid line) and the actual value of the synaptic conductance (black solid line) given as in Figure 11. Panel B represents the scatter plot of the actual versus the estimated synaptic conductance after the interpolation. The red line in panel B is the identity line as a reference to observe the goodness of the estimation. Panel C shows a comparison of the voltages computed using the actual conductance (solid black trace) and the estimated ones (dotted red trace). The other parameter values are $a = 0.25$, $v_0 = 0$, $\gamma = 0.5$, $w_0 = 0$, $v_{\text{syn}} = 0.25 + a/2$, $C = 0.001 \mu\text{F}/\text{cm}^2$, and $I = 0.625 \mu\text{A}/\text{cm}^2$.

5. Discussion. Difficulties in estimating synaptic conductance when the ionic channels of the postsynaptic cell are activated have been extensively reported in the literature (see, for instance, [5], [13], [26], and the references therein). The standard approach of filtering the membrane potential and then fitting the filtered data to a linear model seems to work only in subthreshold regimes with no active ionic currents. In these low-activity regimes it has also been shown that quadratic models improve the estimations in a significant way. In spiking regimes, however, one has to face a greater challenge since the magnitude of ionic currents is far bigger than the magnitude of the synaptic currents. We need, then, a method that is able to disentangle the ionic activity from the synaptic and, at the same time, to extract, from the original recordings, a data set that can be useful to estimate the synaptic input that the cell is receiving. In this manuscript, we have presented a proof of concept of how such methods can be constructed, that is, how nonlinear estimation methods can be implemented in order to estimate synaptic conductance in spiking regimes. Our method relies on the knowledge of the $f - I$ curve of the cell, a nonlinear trait that accounts for the activity of ionic channels involved in the spike generation. The proposed methodology does not take into account other features that could make the estimation more complex, like noise in the system or having other type of nonlinearities.

We have exemplified the general idea with a simple model, the McKean model (1), a piecewise linear version of the FitzHugh–Nagumo system, that allows us to perform analytical computations and give a very accurate approximation of the $f - I$ curve. The strategy proposed

is easily extendable to other models or cell types, where the goodness of the estimations will mainly depend on the accuracy achieved in computing the $f - I$ curve. More precisely, for the McKean model (1), we have restricted to the situation where it exhibits an oscillatory behavior; given a constant value of g_{syn} , we provide an approximation $\hat{T} = \hat{T}(C, I, g_{syn})$ of the period T such that $|T - \hat{T}| = O(C^{0.88})$, which includes the dependence on g_{syn} . This approximation has been obtained by taking into account the flight time of the fast and the slow subperiods. Assuming the parameter g_{syn} to be constant in time, our results show excellent estimations for small values of C (the parameter related to the capacitance) and also for those values of I that are close to the boundaries of the oscillatory regime (see Figure 9). We think that the method could be tested in dynamic-clamp experiments in which the neuron can be first driven to a spiking regime that can be further modulated by a current injection of type $g_{syn}(v - v_{syn})$, with g_{syn} constant.

The estimation procedure also has been extended to a more general and realistic context, where we estimate the time course of variable synaptic conductance. In Figure 10 we show estimations obtained from three different prescribed inputs: a sinusoidal drive, an oscillatory drive with two low frequencies, and a combination of both low and high frequencies. We observe fairly good estimations of synaptic conductance in the first two cases, but the addition of a high frequency makes the estimations poorer. In general, frequencies of the conductance's changes higher than the spike frequency are difficult to estimate. The reconstructed voltage using the estimated conductance (see $v_{rec}(t)$ in the last column in Figure 10) always exhibits a good agreement, meaning that it is not a suitable detector for good estimations. When we inject a stereotypical synaptic input to a single cell in visual cortex taken from a realistic model of V1 (see Figure 11), the estimation captures the overall conductance profile but does not match at a smaller scale. In realistic inputs, the conductance's time-scale is variable, being very short in some moments. Thus, we can only get a good estimation on average.

In order to check the influence of high frequency synaptic inputs, we have improved our method by refining the sampling, taking advantage of the knowledge of the subperiods T_L , T_{Md} , T_{Mu} , and T_R , thus enlarging the sampling set by a factor of 4. Figure 12 compared to the last row of Figure 10 confirms the predicted improvement. For realistic input, however, we appreciate only a slight improvement (see Figure 13 compared to Figure 11).

Summing up, we have shown the viability of the approach based on the use of the $f - I$ curve in order to estimate synaptic conductance in spiking regimes. We have also examined the drawbacks of this proof of concept, but nevertheless we think that our proposal brings up positive results that open new research lines which we aim to address:

- The gain obtained when increasing the sampling indicates that introducing more Poincaré sections to estimate flight times in shorter intervals would be a good strategy to cope with high frequency synaptic inputs. Extending this reasoning to the limit, we plan to add to the model a third differential equation modeling the dynamics of the synaptic conductance. This would allow us to obtain good estimations in a more general context and provide a scheme to be applied to experimental data.
- The scheme need to include both excitatory and inhibitory terms. We have only considered one type of synaptic input. In the examples, we have chosen $v_{syn} = 1/4 + a/2$, a value that could be attributed to excitatory synapses. However, a key aspect

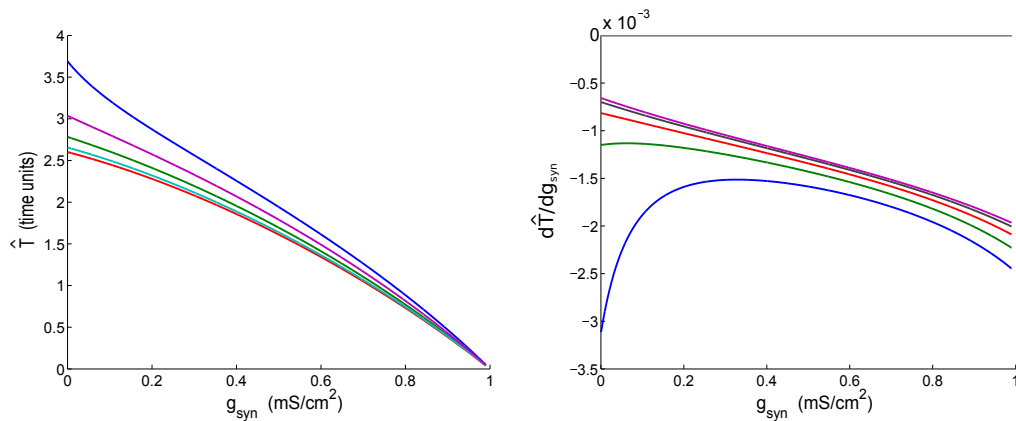


Figure 14. Monotonicity of $\hat{T}(C, I, g_{syn})$ with respect to g_{syn} . This figure shows different plots representing the approximated period \hat{T} and its derivatives versus the synaptic conductance g_{syn} for different values of the applied current. We depict $\hat{T}(g_{syn})$ in panel A and the first derivative $\partial\hat{T}/\partial g_{syn}$ (colored lines) in panel B, together with the line $d\hat{T}/dg_{syn} = 0$ (gray line). The different colored lines, in all panels, stand for different applied currents, namely, $I_{app} \in [0.4, 0.5, 0.6, 0.7, 0.8]$. The rest of parameters of the model are fixed as $C = 1e - 4$, $a = 0.25$, $v_0 = 0$, $w_0 = 0$, $\gamma = 0.5$, and $v_{syn} = 0.25 + a/2$.

in estimating conductance is to differentiate between excitation and inhibition. We think that this step is feasible within the frame of the McKean model.

- The methodology needs to be tested in other conductance-based models with more realistic ionic channels. This extension will require getting approximate expressions of the period in terms of g_{syn} , a challenging problem that can be successfully treated by adapting existing formulas for the period of limit cycles close to bifurcation points; see, for instance, [12].
- Combine the new methodology for spiking regimes with existing estimations for sub-threshold oscillations. This issue connects again with bifurcation diagrams since an ideal method should apply to a variable synaptic input that sweeps the I parameter range from excitable to spiking regimes and vice versa. It also opens an interesting question about the influence of the type of bifurcation (Hopf, saddle-node on invariant curve, etc.) on the goodness of the estimations.

Appendix A. Evidence of the monotonicity of \hat{T} . In Figure 14 we represent the function $\hat{T}(g_{syn})$ (panel A) and the derivative $\partial\hat{T}/\partial g_{syn}$ (panel B) for the set of parameter values used in all the numerical computations, except for the applied current which varies (different colors) in the range of existence of limit cycles. It is worth noting (see, for instance, panel B), that for all the applied currents considered we have that $\partial\hat{T}/\partial g_{syn} < 0$. In all the results given above, we use this numerical evidence together with an on-line check that the derivative does not vanish to ensure that the solution we get from equation (10) is unique.

Appendix B. Numerical methods. In the numerical computations, to solve equation (10) we need the time spent on some trajectory, T^* , that has to be computed numerically. We have computed these values by integrating the orbits and determining the intersection points with the corresponding Poincaré section using both the Newton–Raphson method and the

bisection method with a tolerance $TOL = 1e - 11$ (see Appendix B.1 for more details of the routine). The same methods have been used to estimate the synaptic conductance g_{syn} with tolerance $TOL = C^2$.

In order to integrate the differential piecewise linear system we have used the Runge–Kutta 7-8 method with tolerance $TOL = 1e - 8$ and a maximal step size $h_{max} = 1e - 1$. We have used the `edo78` function of MATLAB.

Finally, we have used the `spline` function of MATLAB to compute the cubic spline interpolation used to construct the continuous time course of the estimated synaptic conductance in Methods 4.1 and 4.2.

B.1. Routine to compute the numerical period. Consider the solution (5) of the model given by the piecewise differential system (1).

- (a) Let $x_0 = (\frac{a}{2}, w_0) = \mathbf{q}_L, \bar{T}_0 = 0$ be the initial condition.
 1. Let x_0 be the initial condition and compute T_{Md} as a zero of the equation $v(t) - \frac{1+a}{2}$. Then, knowing $t = T_{Md}$, we can compute $w_1 = w(T_{Md})$, and so we obtain a new point $x_1 = (\frac{1+a}{2}, w_1)$.
 2. Let x_1 be the initial condition and compute T_R as a zero of the equation $v(t) - \frac{1+a}{2}$. Then, knowing $t = T_R$, we can compute $w_2 = w(T_R)$, and so we obtain a new point $x_2 = (\frac{1+a}{2}, w_2)$.
 3. Let x_2 be the initial condition and compute T_{Mu} as a zero of the equation $v(t) - \frac{a}{2}$. Then, knowing $t = T_{Mu}$, we can compute $w_3 = w(T_{Mu})$, and so we obtain a new point $x_3 = (\frac{1+a}{2}, w_3)$.
 4. Let x_3 be the initial condition and compute T_L as a zero of the equation $v(t) - \frac{a}{2}$. Then, knowing $t = T_L$, we can compute $w_4 = w(T_L)$, and so we obtain a new point $x_4 = (\frac{a}{2}, w_4)$.
 5. Compute $\bar{T} = T_L + T_{Md} + T_R + T_{Mu}$
- (b) If $|w_0 - w_4| < TOL$ or $|\bar{T}_0 - \bar{T}| < TOL$, we are done: the numerical period is \bar{T} . Otherwise, let $x_0 = x_4, \bar{T}_0 = \bar{T}$, and repeat steps 1–5. We have considered $TOL = 1e - 10$ for this step.

REFERENCES

- [1] L. ABBOTT, *A network of oscillators*, J. Phys. A, 23 (1990), p. 3835.
- [2] J. S. ANDERSON, M. CARANDINI, AND D. FERSTER, *Orientation tuning of input conductance, excitation, and inhibition in cat primary visual cortex*, J. Neurophysiology, 84 (2000), pp. 909–926, <https://jn.physiology.org/content/84/2/909.abstract>.
- [3] C. BÉDARD, S. BÉHURET, C. DELEUZE, T. BAL, AND A. DESTEXHE, *Oversampling method to extract excitatory and inhibitory conductances from single-trial membrane potential recordings*, J. Neurosci. Methods, 210 (2012), pp. 3–14, <https://doi.org/10.1016/j.jneumeth.2011.09.010>.
- [4] R. W. BERG AND S. DITLEVSEN, *Synaptic inhibition and excitation estimated via the time constant of membrane potential fluctuations*, J. Neurophysiology, 110 (2013), pp. 1021–1034, <https://doi.org/10.1152/jn.00006.2013>.
- [5] L. BORG-GRAHAM, C. MONIER, AND Y. FRÉGNAC, *Visual input evokes transient and strong shunting inhibition in visual cortical neurons*, Nature, 393 (1998), pp. 369–373, <https://doi.org/10.1038/30735>.
- [6] P. CLOSAS, *Sequential Estimation of Neural Models by Bayesian Filtering*, Diploma thesis, FME-Universitat Politècnica de Catalunya, 2014.

- [7] S. COOMBES, *Phase locking in networks of synaptically coupled mckean relaxation oscillators*, *Phys. D*, 160 (2001), pp. 173–188, [http://dx.doi.org/10.1016/S0167-2789\(01\)00352-9](http://dx.doi.org/10.1016/S0167-2789(01)00352-9).
- [8] S. COOMBES, *Neuronal networks with gap junctions: A study of piecewise linear planar neuron models*, *SIAM J. Appl. Dyn. Syst.*, 7 (2008), pp. 1101–1129, <https://doi.org/10.1137/070707579>.
- [9] S. DITLEVSEN AND A. SAMSON, *Estimation in the partially observed stochastic Morris-Lecar neuronal model with particle filter and stochastic approximation methods*, *Ann. Appl. Stat.*, 8 (2014), pp. 674–702, <https://doi.org/10.1214/14-AOAS729>.
- [10] S. FERNÁNDEZ-GARCÍA, M. DESROCHES, M. KRUPA, AND F. CLÉMENT, *A multiple time scale coupling of piecewise linear oscillators: Application to a neuroendocrine system*, *SIAM J. Appl. Dyn. Syst.*, 14 (2015), pp. 643–673, <https://doi.org/10.1137/140984464>.
- [11] S. FERNÁNDEZ-GARCÍA, M. DESROCHES, M. KRUPA, AND A. TERUEL, *Canard solutions in planar piecewise linear systems with three zones*, *Dyn. Syst.*, 31 (2016), pp. 173–197, <https://doi.org/10.1080/14689367.2015.1079304>.
- [12] A. GASULL, V. MAÑOSA, AND J. VILADELPRAT, *On the period of the limit cycles appearing in one-parameter bifurcations*, *J. Differential Equations*, 213 (2005), pp. 255–288.
- [13] A. GUILLAMON, D. W. MCLAUGHLIN, AND J. RINZEL, *Estimation of synaptic conductances*, *J. Physiology Paris*, 100 (2006), pp. 31–42, <https://doi.org/10.1016/j.jphysparis.2006.09.010>.
- [14] P. HARTMAN, *Ordinary Differential Equations*, 2nd ed., *Classics in Appl. Math.*, SIAM, Philadelphia, 1982, <https://books.google.es/books?id=NEkkJ93O9okC>.
- [15] M. LANKARANY, W. P. ZHU, M. N. S. SWAMY, AND T. TOYOIZUMI, *Inferring trial-to-trial excitatory and inhibitory synaptic inputs from membrane potential using Gaussian mixture Kalman filtering*, *Front. Comput. Neurosci.*, 7 (2013), <https://doi.org/10.3389/fncom.2013.00109>.
- [16] J. LLIBRE, M. ORDÓÑEZ, AND E. PONCE, *On the existence and uniqueness of limit cycles in planar continuous piecewise linear systems without symmetry*, *Nonlinear Anal. Real World Appl.*, 14 (2013), pp. 2002–2012, <http://dx.doi.org/10.1016/j.nonrwa.2013.02.004>.
- [17] H. P. MCKEAN, *Nagumo's equation*, *Adv. Math.*, 4 (1970), pp. 209–223.
- [18] D. MCLAUGHLIN, R. SHAPLEY, M. SHELLEY, AND D. J. WIELAARD, *A neuronal network model of macaque primary visual cortex (V1): Orientation selectivity and dynamics in the input layer 4Calpha*, *Proc. Natl. Acad. Sci. USA*, 97 (2000), pp. 8087–8092, <https://doi.org/10.1073/pnas.110135097>.
- [19] L. PANINSKI, M. VIDNE, B. DEPASQUALE, AND D. G. FERREIRA, *Inferring synaptic inputs given a noisy voltage trace via sequential Monte Carlo methods*, *J. Comput. Neurosci.*, 33 (2012), pp. 1–19, <https://link.springer.com/article/10.1007/s10827-011-0371-7>.
- [20] M. POSPISCHIL, Z. PIWKOWSKA, T. BAL, AND A. DESTEXHE, *Extracting synaptic conductances from single membrane potential traces*, *Neuroscience*, 158 (2009), pp. 545–552.
- [21] R. PROHENS, A. TERUEL, AND C. VICH, *Slowfast n -dimensional piecewise linear differential systems*, *J. Differential Equations*, 260 (2016), pp. 1865–1892, <http://dx.doi.org/10.1016/j.jde.2015.09.046>.
- [22] M. RUDOLPH, Z. PIWKOWSKA, M. BADOUAL, T. BAL, AND A. DESTEXHE, *A method to estimate synaptic conductances from membrane potential fluctuations*, *J. Neurophysiology*, 91 (2004), pp. 2884–2896, <https://doi.org/10.1152/jn.01223.2003>.
- [23] L. TAO, M. SHELLEY, D. MCLAUGHLIN, AND R. SHAPLEY, *An egalitarian network model for the emergence of simple and complex cells in visual cortex*, *Proc. Natl. Acad. Sci. USA*, 101 (2004), pp. 366–371, <https://doi.org/10.1073/pnas.2036460100>.
- [24] A. TONNELIER, *The McKean's caricature of the Fitzhugh–Nagumo model I. The space-clamped system*, *SIAM J. Appl. Math.*, 63 (2003), pp. 459–484, <https://doi.org/10.1137/S0036139901393500>.
- [25] A. TONNELIER AND W. GERSTNER, *Piecewise linear differential equations and integrate-and-fire neurons: Insights from two-dimensional membrane models*, *Phys. Rev. E*, 67 (2003), 21908, <https://doi.org/10.1103/PhysRevE.67.021908>.
- [26] C. VICH AND A. GUILLAMON, *Dissecting estimation of conductances in subthreshold regimes*, *J. Comput. Neurosci.*, 39 (2015), pp. 271–287, <https://doi.org/10.1007/s10827-015-0576-2>.
- [27] M. WEHR AND A. M. ZADOR, *Balanced inhibition underlies tuning and sharpens spike timing in auditory cortex*, *Nature*, 426 (2003), pp. 442–446, <https://doi.org/10.1038/nature02116>.